

Article

Numerical Study on Pressure Pulsation in a Slanted Axial-Flow Pump Device under Partial Loads

Fan Yang ^{1,2,*}, Pengcheng Chang ¹, Wenzhu Hu ¹, Beibei Mao ³, Chao Liu ^{1,4} and Zhongbin Li ¹

- ¹ College of Hydraulic Science and Engineering, Yangzhou University, Yangzhou 225009, China; c1485073308@163.com (P.C.); huhu02@126.com (W.H.); liuchao@yzu.edu.cn (C.L.); yzdxlzb@126.com (Z.L.)
- ² Key Laboratory of Fluid and Power Machinery, Ministry of Education, Chengdu 610039, China
- ³ College of Water Conservancy and Hydropower, Hohai University, Nanjing 210098, China; 180213120007@hhu.edu.cn
- ⁴ Hydrodynamic Engineering Laboratory of Jiangsu Province, Yangzhou University, Yangzhou 225009, China
- * Correspondence: fanyang@yzu.edu.cn

Abstract: The 30° slanted axial-flow pump device is widely used in agricultural irrigation and urban drainage in plains areas of China. However, during the actual operation process, the 30° slanted axial-flow pump device is prone to vibration, noise, cracks in the blades, and other phenomena that affect the safe and stable operation of the pump device. In order to analyze the flow pressure pulsation characteristics of the 30° slanted axial-flow pump device under different flow conditions, the time–frequency domain analysis method was used to analyze the pressure pulsation of each flow structure of the 30° slanted axial-flow pump device. The results showed that the internal pulsation law of the elbow oblique inlet flow channel is similar. At the 1.2 Q_{bep} condition, the amplitude fluctuation of the pressure pulsation was small, and the main frequency is 4 times the rotating frequency. The monitoring points at the outlet of the elbow oblique inlet flow channel were affected by the impeller rotation, and the pressure pulsation amplitude was larger than that inside the elbow oblique inlet flow channel. The pressure fluctuation of each monitoring point at the inlet surface of the impeller was affected by the number of blades. There were four peaks and four valleys, and the main frequency was 4 times the rotating frequency. The amplitude of pressure fluctuation increased gradually from the hub to the rim. The main frequency of pressure fluctuation at each monitoring point of the impeller outlet surface was 4 times of the rotating frequency, and the low frequency was rich. The amplitude of pressure fluctuation was significantly lower than that of the impeller inlet. With the increase of flow rate, the peak fluctuation of pressure coefficient decreased gradually, and the amplitude of pressure fluctuation tended to be stable. Under 0.8 Q_{bep} and 1.0 Q_{bep} conditions, the large fluctuation of the pressure fluctuation amplitude on the outlet surface of the guide vane was mainly affected by the low-frequency fluctuation. Under the 1.2 Q_{bep} condition, the pressure fluctuation amplitude changed periodically.

Keywords: axial flow pump; pump device; pressure pulsation; Fourier transform; numerical simulation; model test



Citation: Yang, F.; Chang, P.; Hu, W.; Mao, B.; Liu, C.; Li, Z. Numerical Study on Pressure Pulsation in a Slanted Axial-Flow Pump Device under Partial Loads. *Processes* **2021**, *9*, 1404. <https://doi.org/10.3390/pr9081404>

Academic Editor: Ambra Giovannelli

Received: 5 July 2021

Accepted: 10 August 2021

Published: 14 August 2021

Publisher's Note: MDPI stays neutral with regard to jurisdictional claims in published maps and institutional affiliations.



Copyright: © 2021 by the authors. Licensee MDPI, Basel, Switzerland. This article is an open access article distributed under the terms and conditions of the Creative Commons Attribution (CC BY) license (<https://creativecommons.org/licenses/by/4.0/>).

1. Introduction

The slanted axial-flow pump device has the characteristics of low head and large flow rate. Because of its simple structure, low cost, small hydraulic loss, high operational reliability, and convenient installation and maintenance, it is widely used in low-head pumping stations in plains areas, which play an important role in improving the disaster resistance and promoting social and economic development in plains areas. At present, the slanted axial-flow pump device is used in ultra-low-lift pumping stations such as Shanghai Jiangzhen River Pump Gate, Hangzhou Sanbao Drainage Pumping Station, Guangdong Guipanhai Pumping Station, and Guangdong Wentouling Pumping Station, which are widely distributed in the Yangtze River Delta and the Pearl River Delta in

China. The 30° slanted axial-flow pump device shown in this paper is one of the slanted axial-flow pump devices and is widely used. The pump stations of Shanghai Diandong Pump Gate, Guangdong Shunde Jingkou Second Pumping Station, and Zhejiang Drainage Sanbao Pumping Station employ the 30° slanted axial-flow pump device. Domestic and foreign scholars have done a lot of research on the slanted axial-flow pump; for example, Zhang et al. [1] numerically simulated the cavitation performance of the slanted axial-flow pump under different working conditions and explored the causes of the collapse of the cavitation performance of the slanted axial-flow pump. Wang et al. [2] found that there was a flow deviation phenomenon in the S-shaped channel of the 15° slanted axial-flow pump, and carried out numerical simulation research and field measurement on the test bench to clarify the mechanism of this phenomenon. Yang et al. [3], based on Reynolds-averaged Navier–Stokes equations and RNG k - ε turbulence model, studied the three-dimensional fluid flow in a slanted axial-flow pump, analyzed the velocity distribution and stress distribution of the flow field in the slanted axial-flow pump under different working conditions, and found that they were in good agreement with the experimental study. Fu et al. [4] studied the transient characteristics of the slanted axial-flow pump in the start-up process, and used a numerical simulation method to simulate the start-up transition process of the slanted axial-flow pump. The results of the latter study could help to avoid the start-up vibration problem in engineering. Kan et al. [5] used the VOF method and RLH method to deal with the free water surface of the slanted axial-flow pump, and compared the advantages and disadvantages of the two water surface treatment methods by numerical simulation, laying the foundation for the study of gas–liquid two-phase flow in the pump device. Wang et al. [6] used an unsteady numerical simulation method to simulate the flow pattern of 15° slanted axial-flow pump, and studied the characteristic curve, pressure fluctuation, and radial force of pump impeller. Zhang et al. [7] studied the influence of different tip clearances on the hydraulic performance of a slanted axial-flow pump by using a curvature-corrected filtering model. Wu et al. [8] designed four relative position schemes of guide vanes to conduct numerical calculation research on an S-type slanted axial-flow pump under different working conditions, and studied the influence of guide vane position on its hydraulic performance. Xie et al. [9] carried out numerical simulation on vertical shaft and slanted axial-flow pump devices. On the premise of maintaining the same hydraulic model and flow channel length, the performance differences between the two were compared to provide reference for pump station selection. Huang et al. [10] used an orthogonal experimental design method to optimize the slanted axial-flow pump device, combined with CFD technology to study the influence of inlet geometry size on pump device performance. Based on CFD technology, Xie et al. [11] studied the cavitation performance and pressure pulsation of an 15° slanted axial-flow pump device and expounded the difference from the vertical axial flow pump. Based on a SST k - ω turbulence model, Tang et al. [12] used RANS and URANS methods to numerically calculate the transient and steady states of the slanted axial-flow pump, and compared the differences in flow pattern and velocity distribution between the two. Wang et al. [13] used three common boundary circulation distribution methods for numerical simulation, and compared the eccentric flow, vortex, and turbulence characteristics of the outlet channel of the slanted axial-flow pump. Combined with experimental comparison, it was found that the numerical reliability of the nonlinear model was good.

In the past, scholars have mainly focused on the flow field in the pump device, the position of the hydraulic model, the cavitation performance and the improvement of the geometric size of the inlet and outlet flow channel. However, there have been few studies on the pressure pulsation analysis of the slanted axial-flow pump device. The internal flow field distribution of the slanted axial-flow pump device is complex, and the pressure pulsation inside the pump device is difficult to measure and the test time is long [14]. Numerical simulation technology is an effective means by which to study the pressure pulsation of a slanted axial-flow pump device. In order to clarify the hydraulic stability and internal flow characteristics of a 30° slanted axial-flow pump device, this paper analyzed

the pressure pulsation of a 30° slanted axial-flow pump device, which provides a theoretical basis for the optimization of the 30° slanted axial-flow pump device.

2. Numerical Calculation and Experimental Verification

2.1. Computation Model

The slanted axial-flow pump device includes four flow passages: elbow oblique inlet flow channel, impeller, guide vane, and straight pipe outlet flow channel. UG software was used to establish a three-dimensional solid model of the elbow oblique inlet flow channel calculation domain and the straight pipe outlet flow channel calculation domain. ANSYS TurboGrid software was used to establish a three-dimensional solid model of the impeller calculation domain and the guide vane calculation domain. The hydraulic model of the slanted axial-flow pump device was ZM3.0-Y991. The design of the ZM3.0 axial flow pump adopts the radial balance equation to calculate the flow and, according to the plane mountain theory, the cascade model is solved by the surface element method [15]. The nominal diameter of the impeller is 1.68 m, the number of impeller blades is 4, the hub ratio is 0.402, the thickness of the blade end is 28.2 mm, and the thickness of the blade root is 52.3 mm. According to the requirements of the water conservancy industry standard of the People's Republic of China *Specification of equipment installation and acceptance for pumping stations* (SL317-2015), the tip clearance is 1.5 mm. The design of the guide vane was carried out directly using a simplified three-dimensional flow model [15], and the number of vanes is five. The rated speed n of the pump device is 250 r/min, the designed flow Q_{bep} is 10.66 m³/s, the rotational frequency is 4.17 Hz, and the blade frequency is 16.67 Hz. The three-dimensional solid model of the pump device is shown in Figure 1, and the geometric dimensions of the elbow oblique inlet flow channel and straight pipe outlet flow channel are shown in Figure 2.

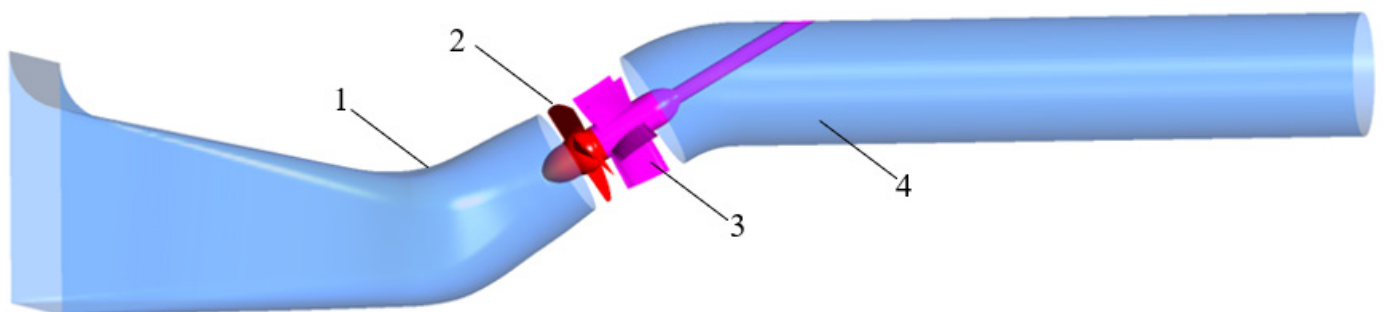


Figure 1. Three-dimensional model of slanted axial-flow pump device. (1) Elbow inlet oblique inlet flow channel, (2) impeller, (3) guide vane, and (4) straight pipe outlet flow channel.

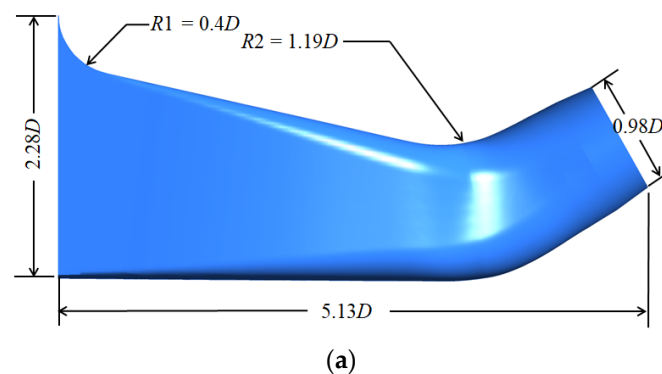


Figure 2. Cont.

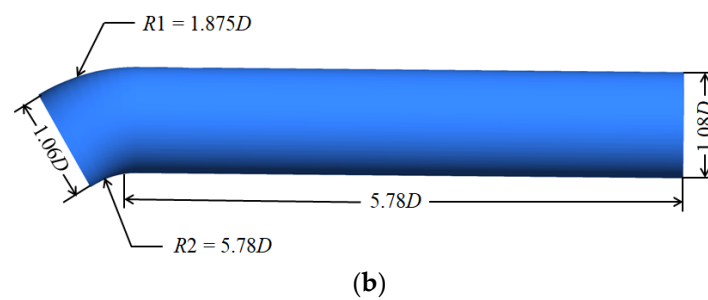


Figure 2. Dimensional drawing of elbow oblique inlet flow channel and straight pipe outlet flow channel. (a) Elbow oblique inlet flow channel, (b) straight pipe outlet flow channel.

2.2. Calculation Method and Boundary Conditions

The RNG $k-\varepsilon$ turbulence model takes into account the rotation and swirl flow in the average flow, and can better deal with flows with a high strain rate and large streamline curvature. It is mainly applied to the flow in rotating coordinate systems. The model can better reflect the dynamic and static interference caused by the rotation of the impeller, and can effectively predict the unsteady three-dimensional flow and pressure pulsation of an axial flow pump device. In References [16–18], the Reynolds-averaged Navier–Stokes equation and RNG $k-\varepsilon$ turbulence model were used to numerically simulate the flow in an oblique 30° axially extended tubular pump. The inlet boundary condition was the flow inlet, the flow rate was set to $10.66 \text{ m}^3/\text{s}$, the outlet boundary condition was the pressure outlet, the pressure value was set to 1 atm, the solid wall was a non-slip wall, and the convergence accuracy was set to 1.0×10^{-5} . The interface between the calculation domain of the impeller and the calculation domain of the inlet channel and the calculation domain of the guide vane body was set as the dynamic and static interface, and the Transient Rotor Stator interface type was used for the unsteady calculation [14,19,20]. The interface of another computing domain was set as the static interface, and the None interface model was adopted. The unsteady constant value simulation of the 30° slanted axial-flow pump device was calculated once every 3° of the impeller rotation [21,22], with one revolution of the impeller taking 120 steps. In order to stabilize the simulation results of the unsteady flow field and control the amount of calculation, the present study calculated eight impeller rotation cycles, a total of 960 steps. According to the pump device speed conversion, the impeller rotation 3° time was 0.002 s and the total time of eight revolutions was 0.92 s. As the rotation time increased, the flow field movement tended to be stable. Therefore, the authors of this paper selected the pressure pulsation data of the last four rotation cycles to analyze the pump device.

2.3. Verification of Grid Number Independence and Convergence

The ICEM CFD software was used to divide the structure grid of the inlet and outlet channels, and the calculation domain of the impeller and the guide vane body were divided into a structural grid using the Ansys TurboGrid software.

The grid independence analysis of the whole pump device was carried out under the optimal working conditions, and the numerical simulation was carried out using eight groups of grids from 1.64 million to 5.14 million. The efficiency calculation results corresponding to different grid numbers were compared and analyzed. The relationship curve between the overall grid number and efficiency of the pump device is shown in Figure 3. It can be seen from Figure 3 that the efficiency of the pump device increased with the increase in the number of grids. When the number of grids ranged from 1.64 million to 4.29 million, the efficiency increase was relatively large; when the number of grids reached 4.29 million, the efficiency change trend tended to be flat. When the number of grids was increased to 4.83 million, the efficiency increase was within 0.3%, which met the accuracy requirements of numerical simulation.

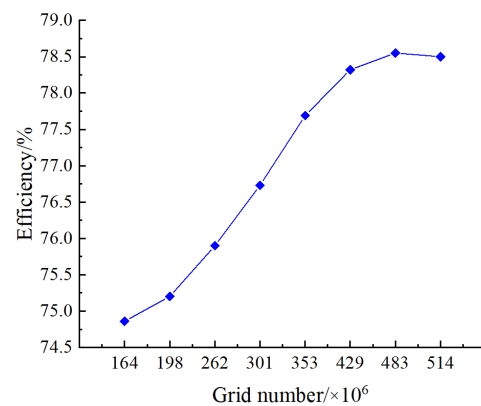


Figure 3. Independence of the number of grids.

In order to further test grid convergence, References [23,24] introduced the grid convergence index GCI (Grid Convergence Index). Using GCI as the criterion, three groups of grids of 4.29 million, 4.83 million, and 5.14 million were selected (Numbers 1–3, respectively). We compared the simulated values and extrapolated values obtained from three groups of different grid numbers and selected a set of appropriate grid numbers to make the numerical simulation solution reach the pseudo-steady-state condition.

According to the calculation steps of GCI in Reference [25], after calculation of $GCI_{21} = 0.02\%$ and $GCI_{32} = 0.02\%$, both GCI_{21} and GCI_{32} were less than 1%, indicating that the discrete error was within a reasonable range [25] and the grid convergence was good. The three groups of grids were suitable for numerical simulation. In view of the fact that the pump device efficiency reached 78.55% when the grid was 4.83 million, the final grid number was 4.83 million.

When designing the flow conditions, the y^+ values of the flow components of the slanted axial-flow pump device studied in this paper were as follows: the elbow oblique inlet flow channel was about 289, the impeller was about 28, and the guide vane body was about 53. The straight pipe outlet flow channel was about 201, which met the requirements of numerical simulation solution [26,27]. The impeller guide vane grid is shown in Figure 4. The impeller mesh details are shown in Figure 5.

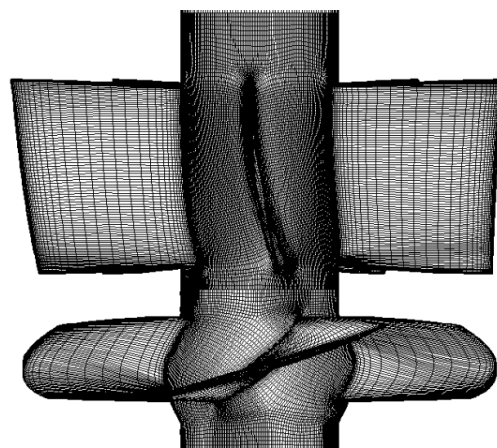


Figure 4. Grid map of impeller guide vanes.

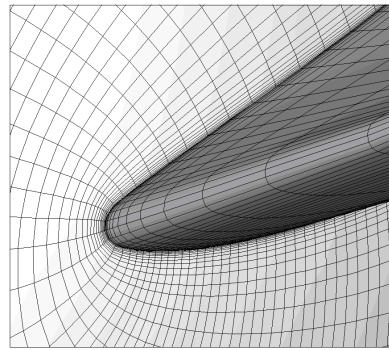


Figure 5. Detailed grid diagram of the impeller.

2.4. Experimental Verification of Numerical Calculations

The physical model test bench of the 30° slanted axial-flow pump device was tested in accordance with the water conservancy industry standard of the People's Republic of China *Code of Practice for Model Pump and Its Installation Acceptance Tests (SL140-2006)*. The nominal diameter of the impeller used in the model test was 300 mm, the rotational speed was 1400 r/min, the number of blades of the impeller was four, the number of blades of the guide blade was five, and the blade placement angle was 0°. The physical model test diagram of the 30° slanted axial-flow pump device is shown in Figure 6. The nD value is another expression of the impeller flange velocity of axial flow pump, which reflects an abstract index of the energy and cavitation characteristics of the pump device. Therefore, the cavitation performance and energy performance of the prototype pump and the model pump should be maintained with the same cavitation performance and energy performance, so that the nD value of the model pump and the prototype pump is equal. In order to verify the reliability of the numerical simulation, the geometric size of the prototype pump device was converted to the model according to the principle of equal nD value. The impeller speed of the converted physical model pump device was 1400 r/min and the nominal diameter of the impeller was 0.3 m. The prototype of the flow structure was scaled to the model according to the scale of 0.1786. Under the condition of 0° blade placement angle, the head and efficiency of the pump device model under different flow conditions were collected. The equivalent efficiency conversion method was used to convert the physical model test results of the pump device to the prototype. The performance results of the converted physical model were compared with the energy performance results of the numerical simulation, as shown in Figure 7. The variation trend of the performance curve predicted by the model of the 30° slanted axial-flow pump device studied in this paper was basically consistent with that of the test curve. The maximum difference between the head of the pump device predicted by the numerical simulation and the physical model test was 4.0%, and the minimum difference was 1.2%. The maximum difference between the efficiency of the pump device predicted by the numerical simulation and the physical model test was 5.88%, and the minimum difference was 0.3%. The small error indicates the effectiveness and reliability of the numerical simulation of the 30° slanted axial-flow pump device.

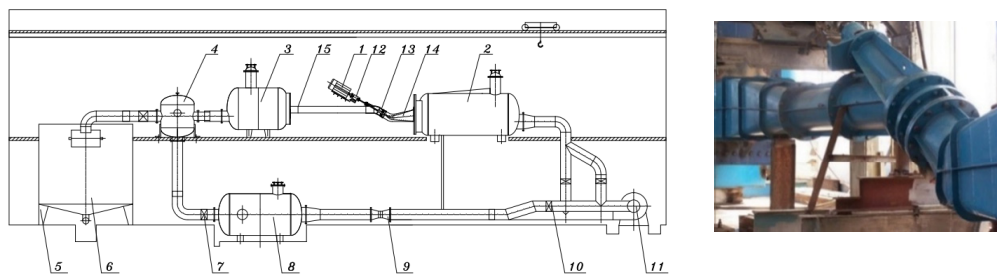


Figure 6. Physical model test diagram of inclined axial extended tubular pump: (1) motor, (2) intake tank, (3) pressure outlet tank, (4) bifurcation tank, (5) load cell, (6) in situ calibration device, (7) regulating gate valve, (8) voltage regulator rectifier tube, (9) electromagnetic flowmeter, (10) control gate valve, (11) auxiliary pump unit, (12) torsigraph, (13) pump test device, (14) inlet flow channel, (15) outlet flow channel.

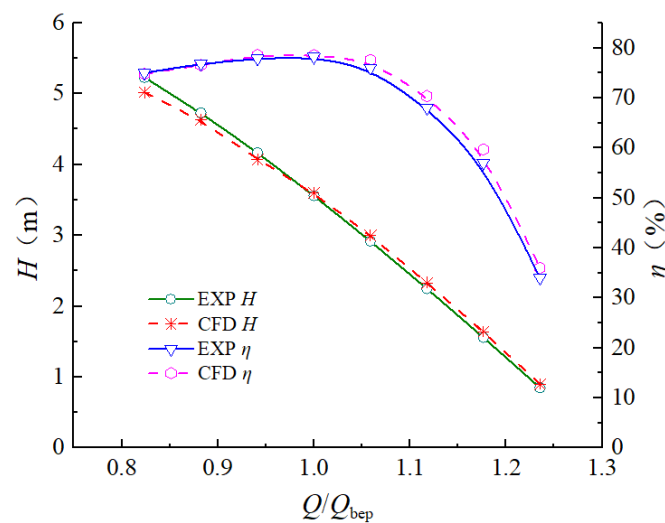


Figure 7. Comparison of energy performance between model test and numerical simulation.

2.5. Pressure Pulsation Monitoring Point Layout

In order to monitor and analyze the pressure fluctuation in the inlet and outlet passages and the blade area of the slanted axial-flow pump device, a total of 19 pressure fluctuation monitoring points were set up. The monitoring points were arranged as shown in Figure 8. Six monitoring points were arranged in the elbow oblique inlet flow channel passage: Monitoring points 1 and 4 were $0.417D$ from the impeller center line, monitoring points 2 and 5 were $0.595D$ from the impeller center line, and monitoring points 3 and 6 were $0.833D$ from the impeller center line. The pressure pulsation monitoring points P7–P9 were arranged at the impeller inlet (distance from the impeller centerline $0.167D$), and the pressure pulsation monitoring points P10–P12 were arranged at the interface between the impeller and the guide vane body (distance from the impeller centerline $0.167D$). Pressure pulsation monitoring points P13–P15 were arranged at the outlet of the body ($0.76D$ from the centerline of the impeller), and the three cross-section pressure pulsation monitoring points were equidistantly distributed. The pressure pulsation monitoring points P7–P9 were arranged at the impeller inlet (distance from the impeller centerline $0.167D$), and the pressure pulsation monitoring points P10–P12 were arranged at the interface between the impeller and the guide vane body (distance from the impeller centerline $0.167D$). Pressure pulsation monitoring points P13–P15 were arranged at the outlet of the body ($0.76D$ from the centerline of the impeller), and the three cross-section pressure pulsation monitoring points were equidistantly distributed. Four monitoring points were arranged in the straight pipe outlet flow channel. Monitoring points 16 and 18 were $1.190D$ away from the impeller center line, and monitoring points 17 and 19 were $4.727D$ away from the outlet section of the slanted axial-flow pump device.

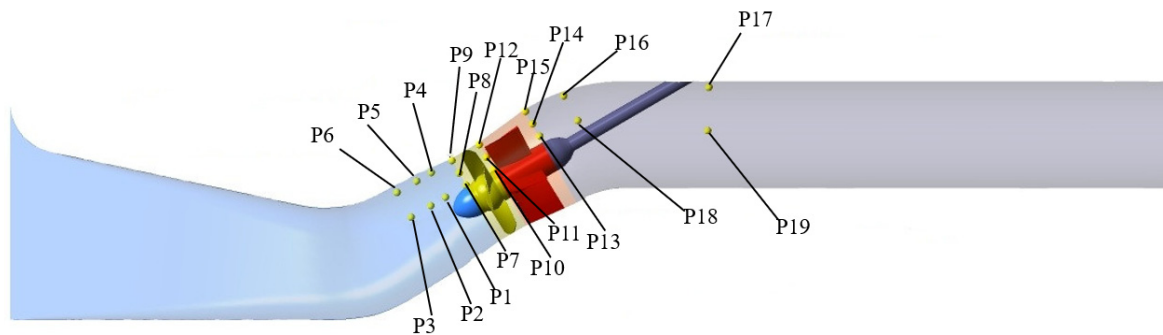


Figure 8. Position diagram of pressure fluctuation monitoring points.

3. Time–Frequency Analysis of Pressure Pulsation

3.1. Time Domain Analysis of Pressure Pulsation

According to Reference [28], this paper selected $0.8 Q_{\text{bep}}$, $1.0 Q_{\text{bep}}$, and $1.2 Q_{\text{bep}}$ as the three flow conditions of pressure pulsation for analysis. The pressure pulsation analysis method is divided into the time domain method and the frequency domain method. The time domain is a real domain, where the independent variable is time and the dependent variable is signal data. The dependent variable in this paper was the pressure value. In the process of time domain analysis, in order to eliminate the static pressure and other interference, it was necessary to deal with the instantaneous pressure dimensionlessly. References [29,30] introduced the pressure coefficient C_p , for which the expression is as follows:

$$C_p = \frac{p - \bar{p}}{0.5\rho u_2^2} \quad (1)$$

where p is the transient pressure value in Pa, \bar{p} is the average pressure value in Pa, ρ is the density of water in kg/m^3 , and u_2 is the impeller outlet circumferential velocity in m/s.

Figure 9 shows the time domain diagrams of the pressure fluctuation of the monitoring points 1–3 in the elbow oblique inlet flow channel. Monitoring points 1–3 were located at the hub side. At each flow condition, the pressure law and pressure value of the monitoring points 1–3 were approximately equal, and the distance from the monitoring point to the impeller inlet section had no obvious effect on the pressure of the monitoring point. The pressure coefficient of monitoring points 1–3 was in the range of -0.0005 – 0.0005 , and did not change greatly with the change of flow rate. Under the condition of $0.8 Q_{\text{bep}}$, the pressure fluctuation range in four rotation cycles was large and did not show regularity. Under the condition of $1.0 Q_{\text{bep}}$, the fluctuation range of the maximum and minimum values in the pressure fluctuation time domain diagram was significantly improved compared with that under the condition of $0.8 Q_{\text{bep}}$. When the flow rate increased to $1.2 Q_{\text{bep}}$, the pressure pulsation of monitoring points 1–3 had a strong regularity, and there were four peaks and four troughs in a rotation cycle, indicating that the pressure of monitoring points 1–3 was affected by the impeller rotation under the $1.2 Q_{\text{bep}}$ condition.

Figure 10 shows the pressure pulsation time domain diagrams of the elbow oblique inlet flow channel monitoring points 4–6. Monitoring points 4–6 were located on the side of the wheel flange. Under the $0.8 Q_{\text{bep}}$ and $1.0 Q_{\text{bep}}$ working conditions, monitoring points 4–6 were better than the other monitoring points. There were obvious regularities in the results of monitoring points 1–3, indicating that the rim side of the elbow-shaped inclined water inlet channel was more affected by the rotation of the impeller than the hub side. The pressure fluctuation of monitoring points 4–6 gradually tended to become stable with the increase of flow rate. Monitoring point 4 was closest to the impeller inlet section, and its pressure change was significantly affected by the impeller rotation. The absolute values of the maximum and minimum pressure pulsation coefficients were greater than the pressure pulsation coefficients under various flow conditions. In one rotation cycle, the pressure pulsation of monitoring point 4 had four peaks and four troughs. Monitoring

points 5 and 6 were far away from the impeller inlet section, and the pressure fluctuation fluctuated periodically under the $1.2 Q_{bep}$ condition.

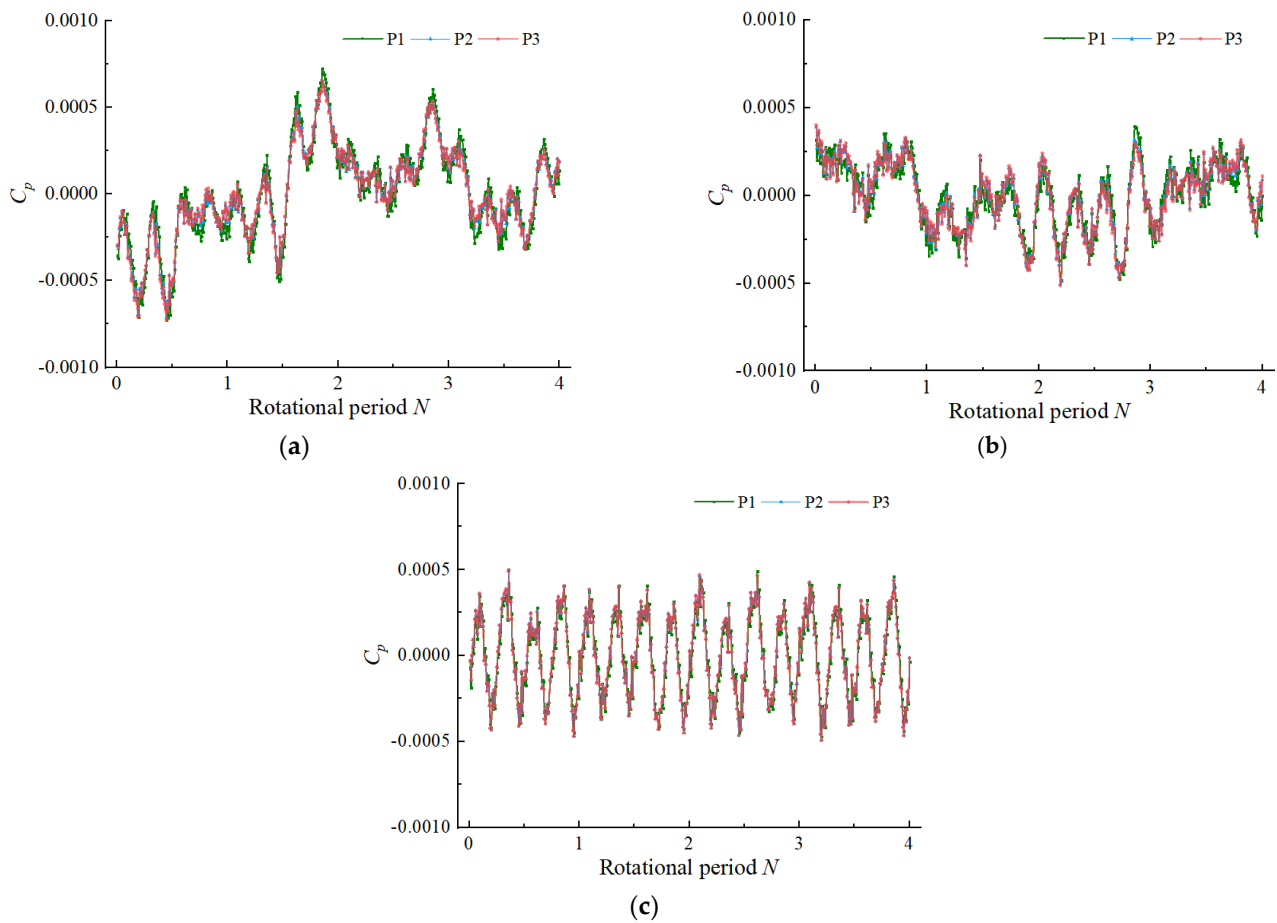


Figure 9. Time domain diagram of P1–3 pressure fluctuations at elbow oblique inlet flow channel monitoring points: (a) $0.8 Q_{bep}$, (b) $1.0 Q_{bep}$, (c) $1.2 Q_{bep}$.

Figure 11 shows the pressure fluctuation time domain diagrams of the impeller inlet monitoring points under different flow conditions. It can be seen that the pressure fluctuation at the monitoring points of the impeller inlet section was relatively regular, forming a sine wave shape with obvious periodicity. In each rotation cycle, there were four peaks and four troughs, and the peaks and troughs appeared at roughly the same time. This is because the impeller rotates and the pressure produces alternating fluctuations. Although the flow at the impeller inlet section does not enter the impeller rotating channel, the impeller rotation affects the flow at the impeller inlet and outlet channels. The number of impeller blades in the pump device was four, which was consistent with the number of peaks and troughs, indicating that the impeller inlet pressure pulsation was affected by the number of impeller blades. The pressure pulsation amplitude increased from the impeller hub (monitoring point P1) to the flange (monitoring point P3). Under the $0.8 Q_{bep}$ working condition, the pressure pulsation amplitude at the flange was about 2.68 times that at the hub, and 1.25 times that at the middle point of the flow channel. Under the condition of $1.0 Q_{bep}$, the pressure pulsation amplitude at the flange was about 1.5 times that at the hub, and 1.4 times that at the middle point of the flow channel. Under the $1.2 Q_{bep}$ condition, the pressure fluctuation amplitude at the flange was about 3.58 times that at the hub, and 1.55 times that at the middle point of the flow channel. Under the $0.8 Q_{bep}$ condition, the pressure pulsation amplitude of each monitoring point at the impeller inlet was the highest, being significantly higher than that under the design flow condition. With the increase of

flow rate, the pressure pulsation amplitude at the impeller inlet fluctuated slightly and tended to be stable.

Figure 12 shows the time domain diagrams of pressure fluctuation at each monitoring point of the impeller outlet under different flow conditions. At the impeller outlet, the flow was still obviously affected by the impeller rotation, and there were also four peaks and four troughs in each rotation cycle. The guide vane blade is fixed on the hub, which changes the flow direction, makes the spiral flow advance axially, and recovers kinetic energy. Under the guide vane interference, the maximum pressure amplitude at the impeller outlet decreased significantly, which decreased by about 30% under the $0.8 Q_{bep}$ condition, by about 53.5% under the $1.0 Q_{bep}$ condition, and by about 58.7% under the $1.2 Q_{bep}$ condition. Under the influence of static and dynamic interference, the flow at the impeller outlet was unstable, and the pressure fluctuation amplitude fluctuated. With the increase of flow rate, the fluctuation decreased gradually. Under the condition of $0.8 Q_{bep}$, the pressure fluctuation amplitude increased from the hub to the rim. The pressure fluctuation amplitude at the rim was about 1.86 times that at the hub, and 1.45 times that at the middle point of the flow channel. Under the $1.0 Q_{bep}$ condition, the pressure fluctuation amplitude at the flange decreased. Under the $1.2 Q_{bep}$ condition, the pressure fluctuation law was similar to that under the $1.0 Q_{bep}$ condition and the fluctuation amplitude was small. The pressure fluctuation amplitude at the hub was about 1.34 times that at the flange.

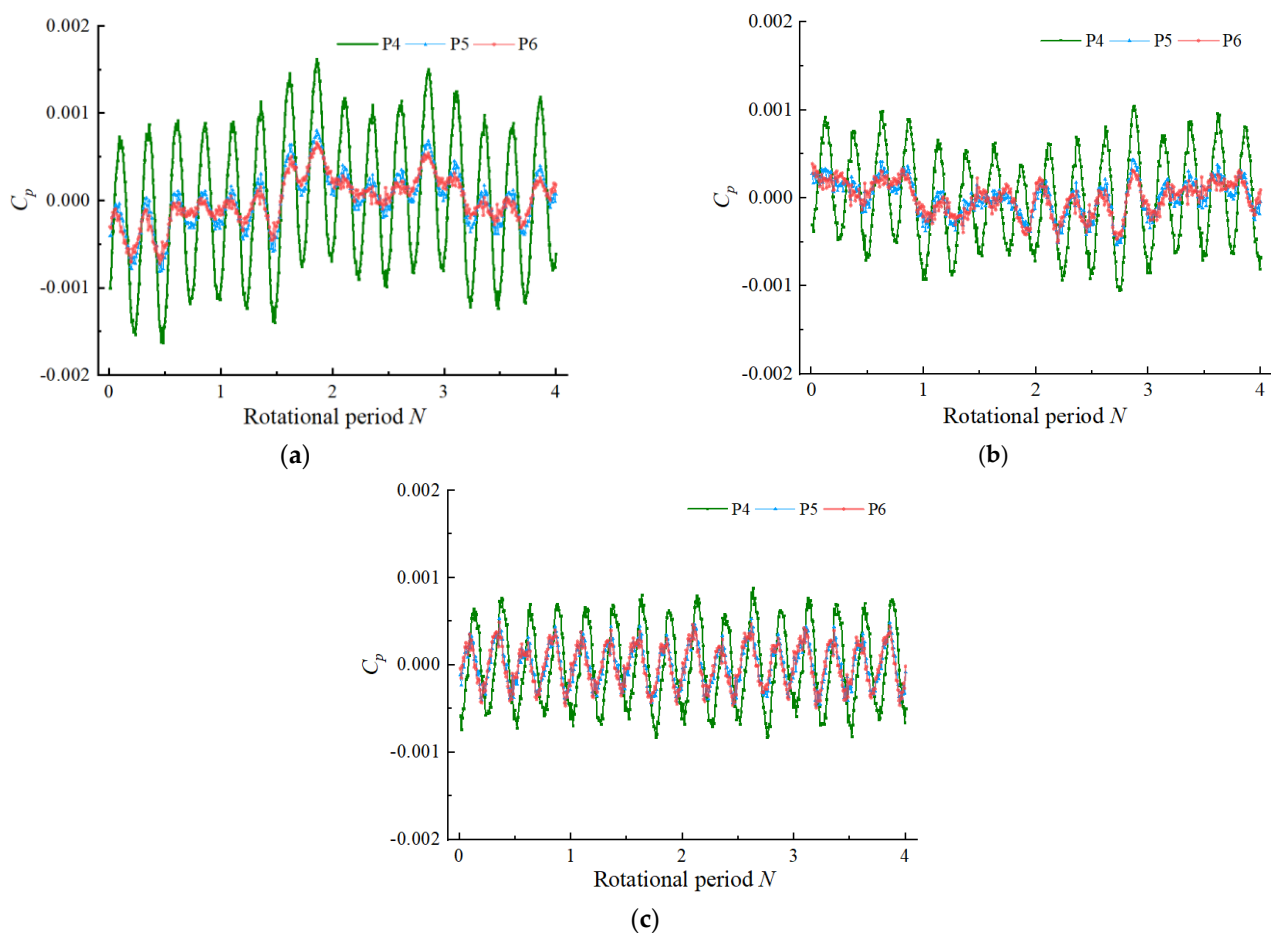


Figure 10. Time domain diagram of P4–6 pressure fluctuation at elbow oblique inlet flow channel monitoring points: (a) $0.8 Q_{bep}$, (b) $1.0 Q_{bep}$, (c) $1.2 Q_{bep}$.

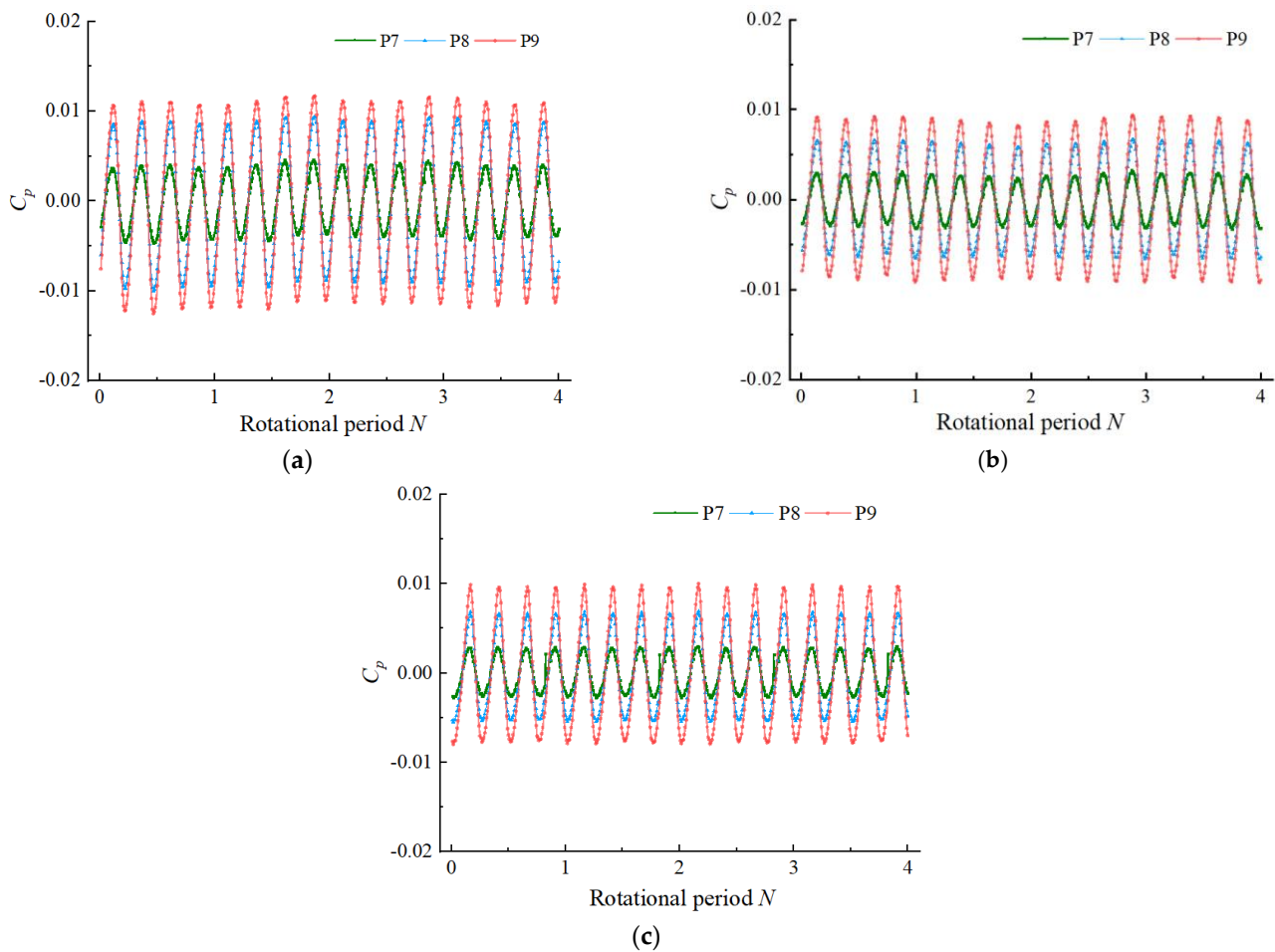


Figure 11. Time domain diagram of pressure fluctuation at impeller inlet: (a) $0.8 Q_{bep}$, (b) $1.0 Q_{bep}$, (c) $1.2 Q_{bep}$.

Figure 13 shows the time domain diagrams of pressure fluctuation at each monitoring point of the guide vane outlet under different flow conditions. Under each flow condition, the amplitude of pressure pulsation at the outlet of the guide vane was similar. It can be seen from Figure 13a,b that under small flow conditions and the $1.0 Q_{bep}$ condition, the pressure pulsation law at the outlet of the guide vane showed a great change compared with the inlet and outlet section of the impeller. Under the $0.8 Q_{bep}$ working condition, the pressure pulsation amplitude of the three monitoring points at the guide vane outlet was significantly decreased compared with that at the impeller outlet, and there was a large fluctuation. The pressure pulsation amplitude at the hub and flange was larger than that at the intermediate point. Under the $1.0 Q_{bep}$ condition, the pressure fluctuation amplitude at hub and flange of guide vane outlet was small. Under the $1.2 Q_{bep}$ condition, the pressure fluctuation at the outlet of the guide vane was still periodic, and there were four peaks and four valleys in one rotation cycle, which indicates that the pressure fluctuation was still greatly affected by the impeller rotation. The pressure fluctuation amplitude at the middle points of the flow channel was greater than that of the other two monitoring points, and the pressure fluctuation law at the hub and rim was similar.

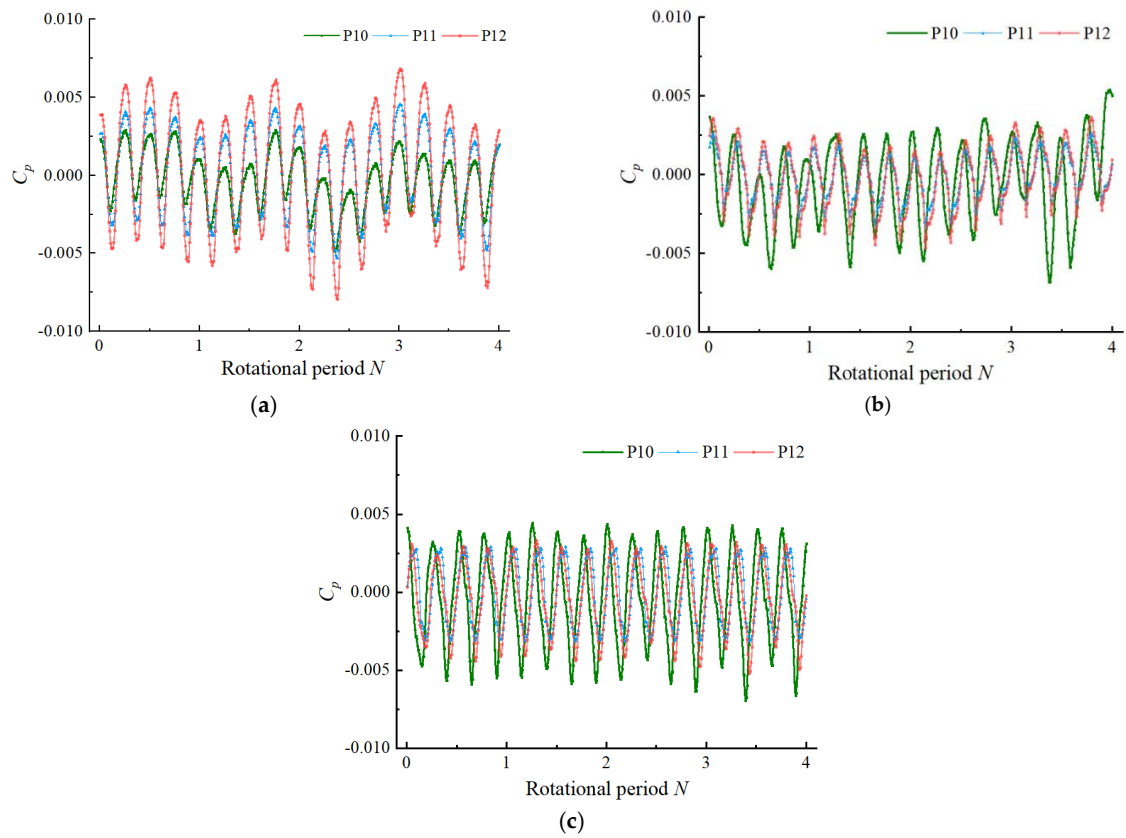


Figure 12. Time domain diagram of impeller outlet pressure fluctuation: (a) $0.8 Q_{bep}$, (b) $1.0 Q_{bep}$, (c) $1.2 Q_{bep}$.

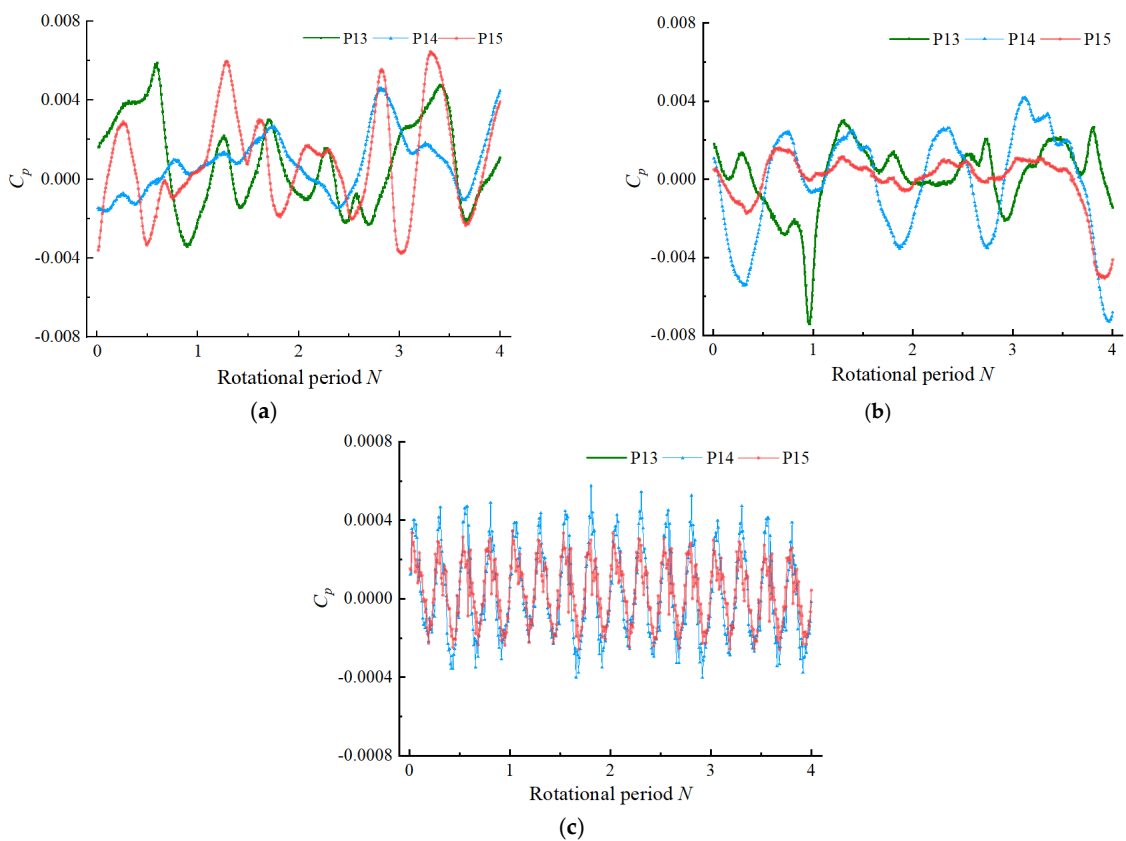


Figure 13. Time domain diagram of pressure fluctuation at guide vane outlet: (a) $0.8 Q_{bep}$, (b) $1.0 Q_{bep}$, (c) $1.2 Q_{bep}$.

Monitoring points 16 and 17 were located at the center of the straight pipe outlet flow channel, for which the pressure fluctuation time domain diagram is shown in Figure 14. Monitoring points 18 and 19 were located at the boundary of straight pipe outlet flow channel, for which the time domain diagram of pressure fluctuation is shown in Figure 15. Monitoring point 16 was close to the outlet section of the guide vane. Affected by the residual circulation, there was one extremum in each rotation cycle under $0.8 Q_{\text{bep}}$ and $1.0 Q_{\text{bep}}$ conditions. Monitoring point 17 was far from the outlet section of the guide vane and the pressure fluctuation was small. With the increase of flow rate, the maximum pressure coefficients of monitoring point 16 and monitoring point 17 decreased significantly. Under the $1.2 Q_{\text{bep}}$ condition, the pressure fluctuation coefficient fluctuated around 0, and the fluctuation was more severe than that under the $0.8 Q_{\text{bep}}$ and $1.0 Q_{\text{bep}}$ conditions. Monitoring point 18 was affected by the residual circulation; under the conditions of $0.8 Q_{\text{bep}}$ and $1.0 Q_{\text{bep}}$, the fluctuation amplitude of pressure pulsation was more obvious than that of monitoring point 19. Under the condition of $1.2 Q_{\text{bep}}$, there were four peaks and four troughs in a rotating shaft. The fluctuation amplitude of monitoring point 19 increased with the increase of flow rate.

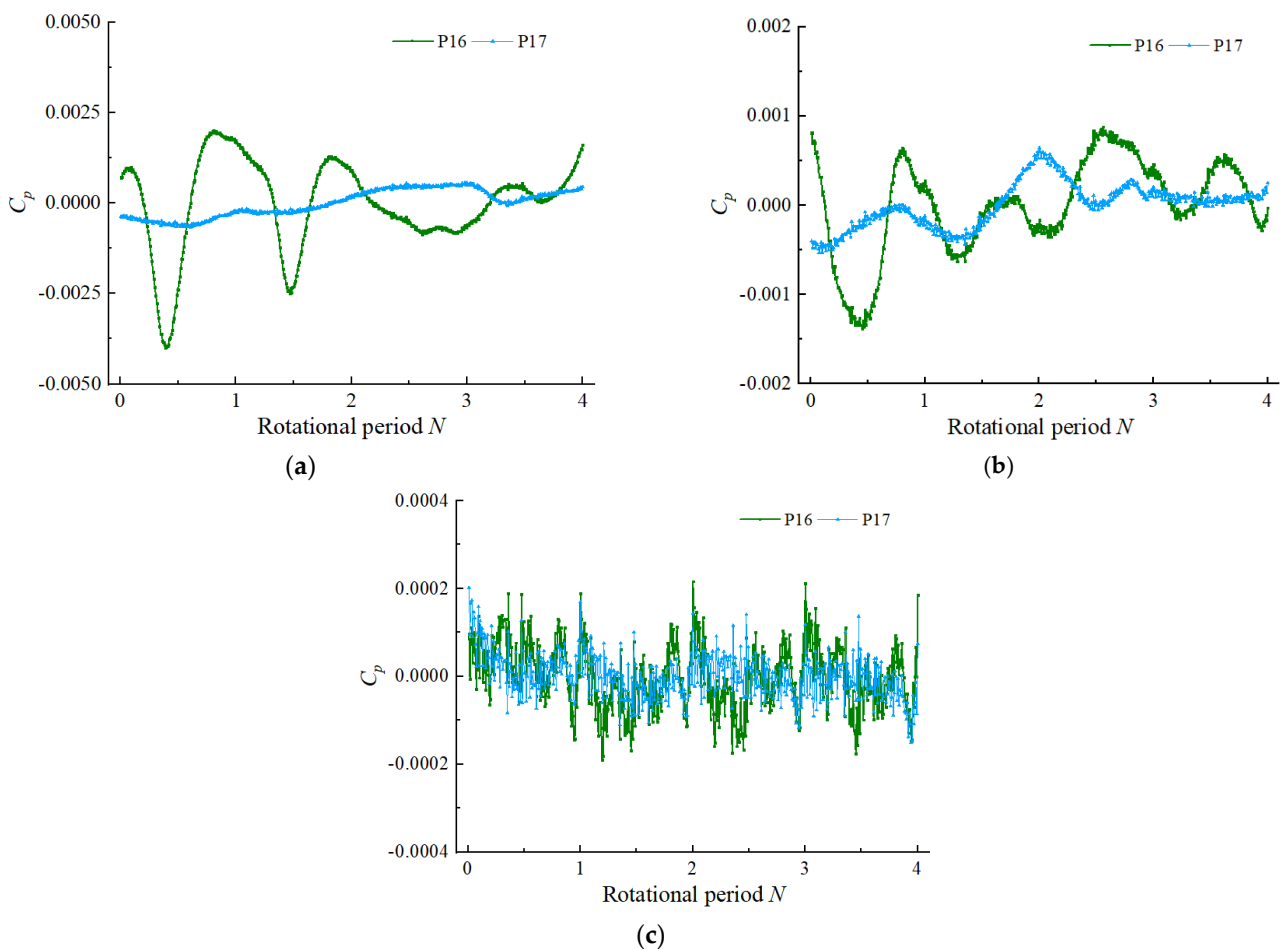


Figure 14. Time domain diagram of pressure fluctuation at monitoring points 16–17 of the straight pipe outlet flow channel: (a) $0.8 Q_{\text{bep}}$, (b) $1.0 Q_{\text{bep}}$, (c) $1.2 Q_{\text{bep}}$.

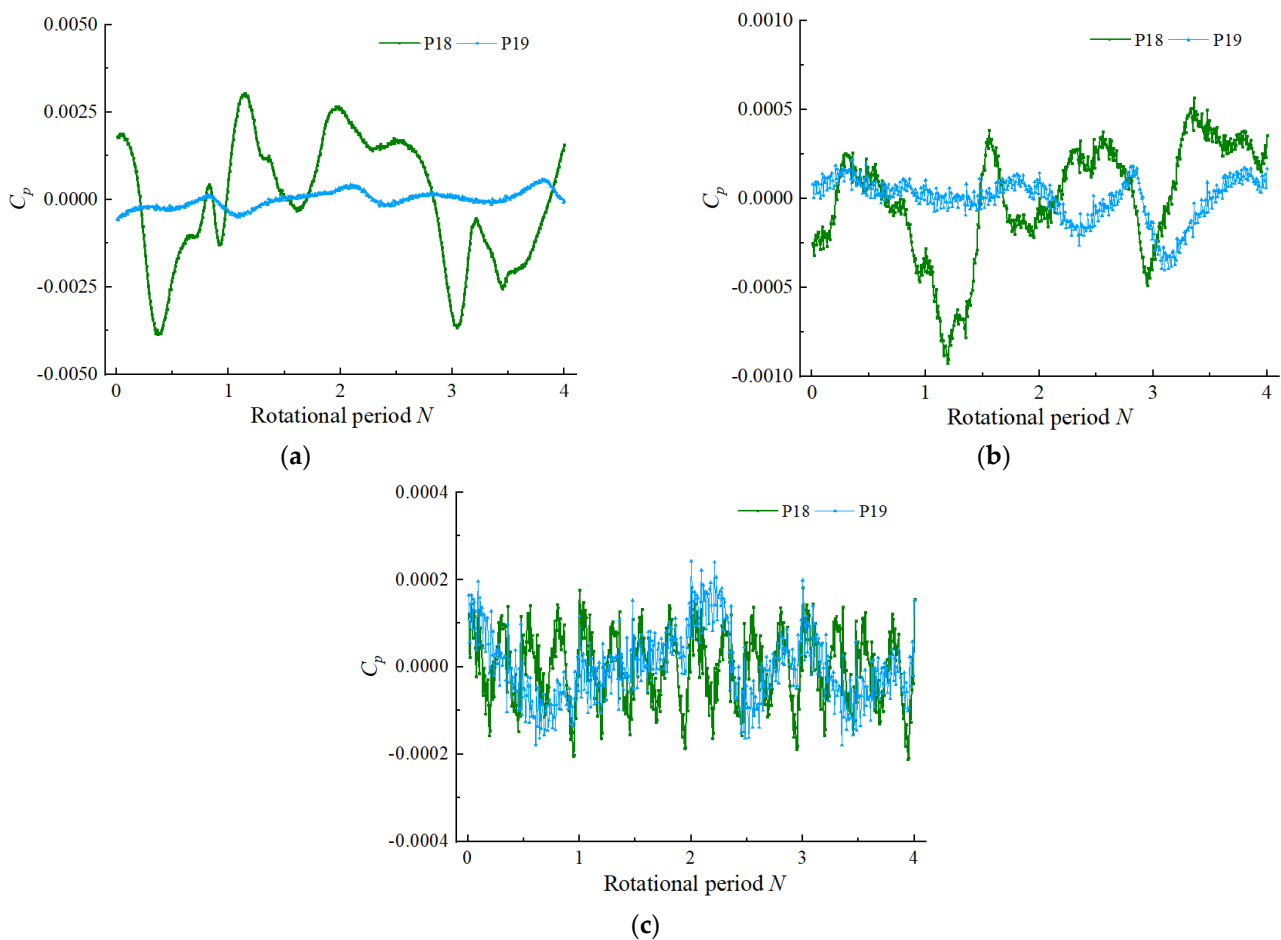


Figure 15. Time domain diagram of pressure fluctuation at monitoring points 18–19 of the straight pipe outlet flow channel: (a) $0.8 Q_{bep}$, (b) $1.0 Q_{bep}$, (c) $1.2 Q_{bep}$.

3.2. Frequency Domain Analysis of Pressure Pulsation

Time domain analysis can be used to analyze data with obvious characteristics, but some signals have the same time domain parameters while other parameters are not exactly the same. It is then necessary to introduce the concept of frequency domain to further analyze the signal. In this paper, FFT was used to analyze the pressure fluctuation in the frequency domain [31,32].

Figure 16 shows the pressure fluctuation spectra of monitoring points 1–3. Under each flow condition, the pressure fluctuation spectra of the three monitoring points had the same law. The low-frequency fluctuation components under the $0.8 Q_{bep}$ and $1.0 Q_{bep}$ conditions were richer than those under the $1.2 Q_{bep}$ condition. Under the $1.2 Q_{bep}$ condition, the main frequency was 4 times the turn frequency. Figure 17 shows the pressure fluctuation spectra of monitoring points 4–6. Monitoring points 4–6 were located in the elbow oblique inlet flow channel near the impeller hub, and the pressure coefficient amplitude was increased compared with the monitoring points 1–3. Under the $0.8 Q_{bep}$ and $1.0 Q_{bep}$ conditions, monitoring point 4 was close to the impeller inlet section, which was greatly affected by the impeller rotation, and the pressure coefficient amplitude corresponding to the main frequency was the largest, reaching 4.5 times those of monitoring point 5 and 6. Under the $1.2 Q_{bep}$ condition, the main frequencies of monitoring point 4–6 were 4 times the turn frequency, and the low-frequency pulsation components were reduced compared with those under the $0.8 Q_{bep}$ and $1.0 Q_{bep}$ conditions. The maximum pressure coefficient amplitude of monitoring point 4 was about 2 times those of monitoring point 5 and monitoring point 6. Under the three flow conditions, the difference in the spectrum

law between monitoring point 5 and monitoring point 6 was small, being less affected by the distance from the impeller inlet section.

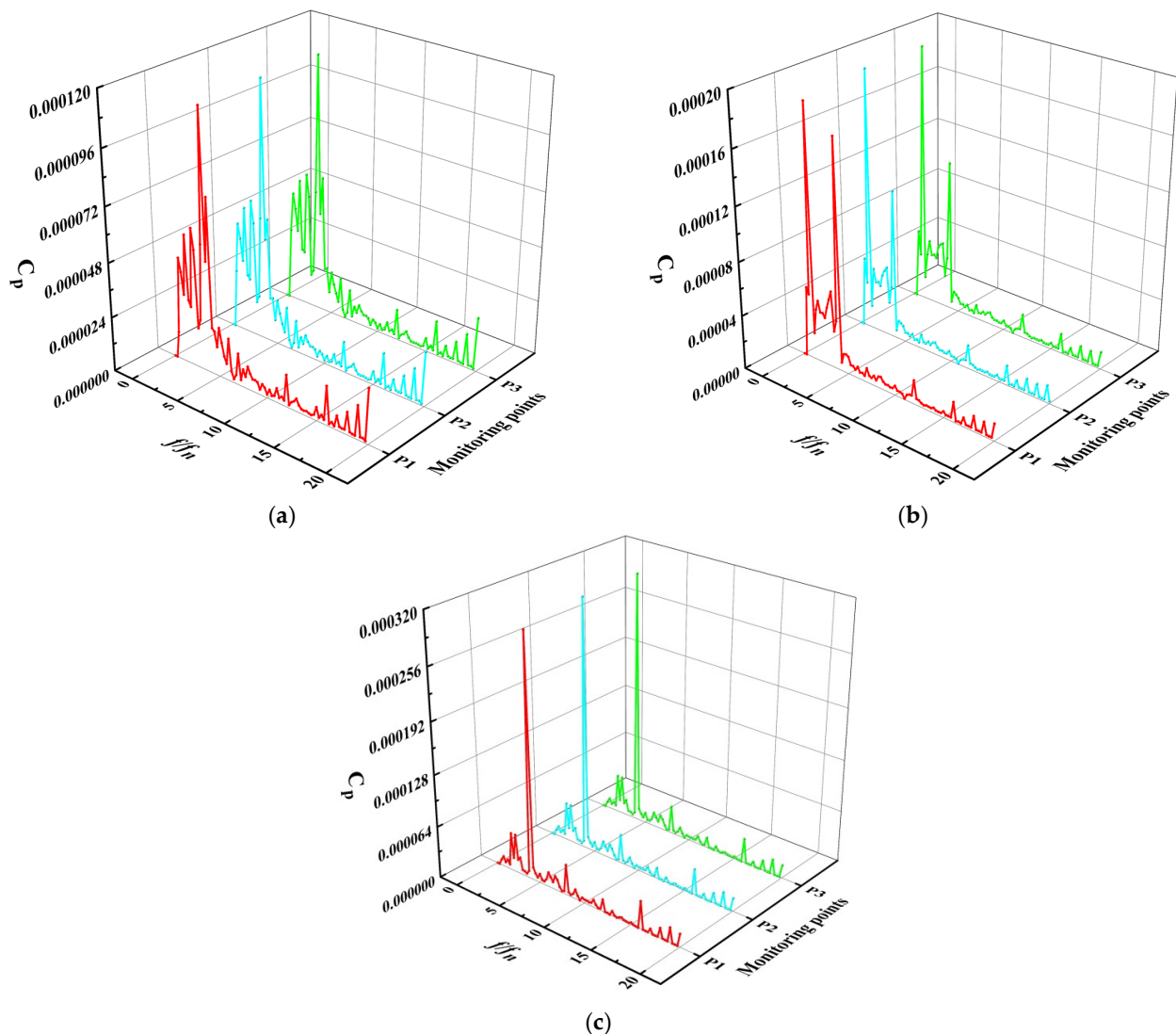


Figure 16. Spectrum diagrams of monitoring points 1–3 of elbow oblique inlet flow channel: (a) $0.8 Q_{bep}$, (b) $1.0 Q_{bep}$, (c) $1.2 Q_{bep}$.

Figure 18 shows the pressure pulsation frequency spectra at each monitoring point of the impeller inlet under different flow conditions. Under different flow conditions, the frequency domain law of pressure fluctuation at the inlet section of the impeller was similar, and the amplitude of pressure fluctuation increased from the hub to the rim. Under the $0.8 Q_{bep}$ condition, the amplitude of pressure fluctuation at the rim reached 3.02 times that at the hub, and 1.4 times that at the middle monitoring point of the flow channel. Under the $1.0 Q_{bep}$ condition, the pressure fluctuation amplitude at the rim reached 2.95 times that at the hub, and 1.34 times that at the middle monitoring point of the flow channel. The main frequency of each monitoring point was located at 4 times the rotating frequency, and the second main frequency was located at 8 times the rotating frequency. The middle monitoring point of the flow channel and the monitoring point of the rim had a large frequency division amplitude at 12 times the rotating frequency, indicating that the number of impeller blades had a significant impact on the pressure fluctuation of the impeller inlet. With the increase of flow rate, the pressure pulsation amplitude of each monitoring point decreased to varying degrees. The pressure pulsation amplitude at the flange under the $1.0 Q_{bep}$ condition was about 32.5% lower than that under the $0.8 Q_{bep}$ condition. The

pressure pulsation amplitude at the intermediate monitoring point of the flow channel was about 30% lower than that under the $0.8 Q_{bep}$ condition. The pressure pulsation amplitude at the hub was about 28.51% lower than that under the $0.8 Q_{bep}$ condition. The pressure pulsation amplitude under the $1.2 Q_{bep}$ condition was lower than that under the $1.0 Q_{bep}$ condition. In Reference [33], the main frequency of each monitoring point at the impeller inlet was consistent with the experimental results of pressure pulsation of the real slanted axial-flow pump, indicating the reliability of numerical calculation.

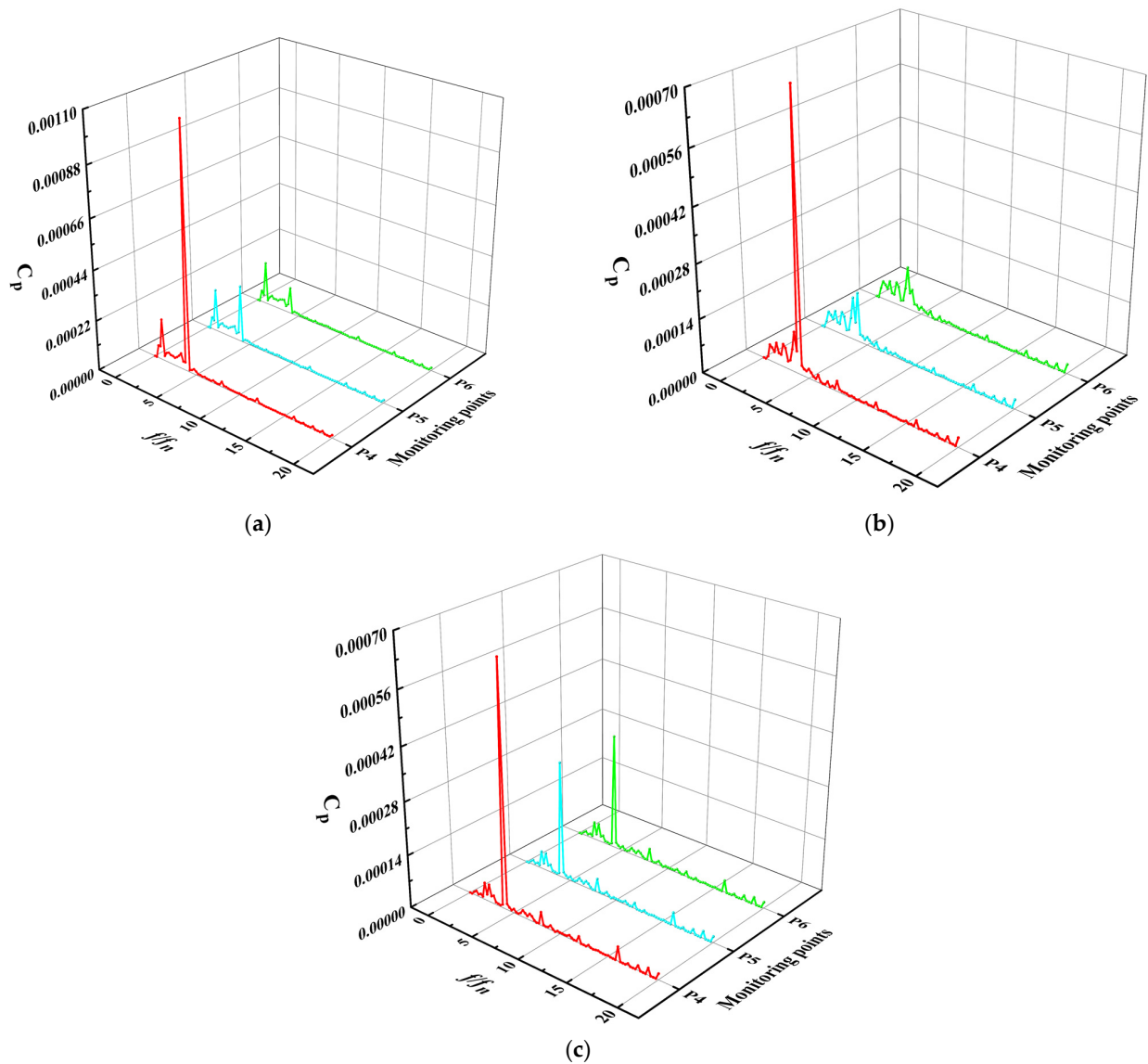


Figure 17. Spectra of monitoring points 4–6 of elbow oblique inlet flow channel: (a) $0.8 Q_{bep}$, (b) $1.0 Q_{bep}$, (c) $1.2 Q_{bep}$.

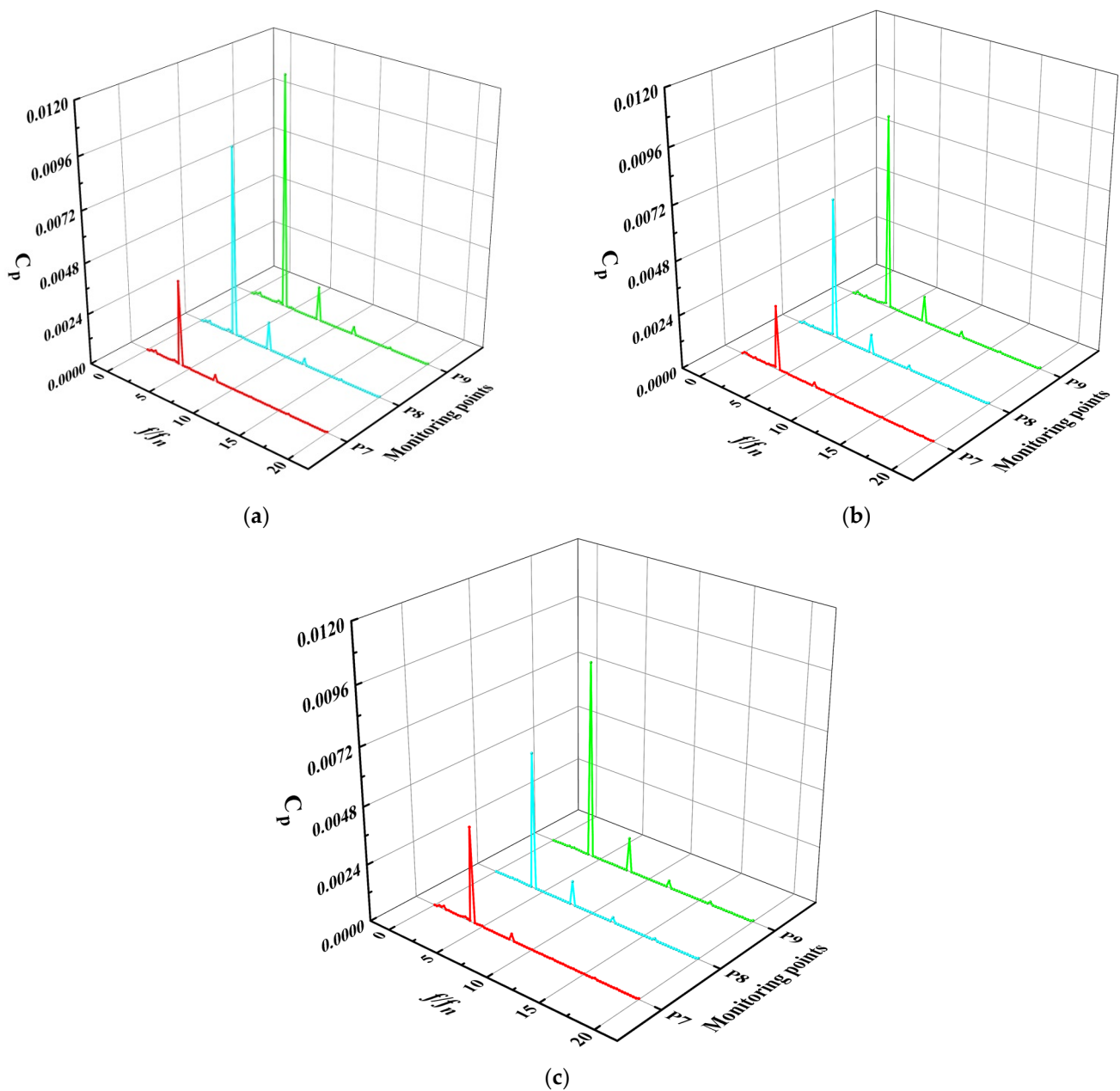


Figure 18. Spectra of pressure fluctuation at impeller inlet: (a) $0.8 Q_{bep}$, (b) $1.0 Q_{bep}$, (c) $1.2 Q_{bep}$.

Figure 19 shows the spectra of pressure fluctuation at each monitoring point of the impeller outlet under different flow conditions. Compared with the impeller inlet, the impeller outlet pressure under different flow conditions did not show an obvious law, and the low-frequency pulsation was more abundant. The pressure pulsation at each monitoring point was still affected by the number of impeller blades, and the main frequency appeared at a frequency of 4. Under the $0.8 Q_{bep}$ working condition, the pressure pulsation amplitude of the impeller increased from the hub to the flange. The pressure pulsation amplitude at the flange was about 3.01 times that at the hub and 1.59 times that at the middle point of the flow channel. The second main frequency appeared at the frequency of 0.75, and there was a large frequency division amplitude at the frequency of 8. Under the $1.0 Q_{bep}$ condition, the low-frequency pulsation occurred at the hub and flange of the impeller. The pressure pulsation amplitude at the hub was the largest: 1.77 times that at the middle point of the flow channel and 1.3 times that at the flange. Under the $1.2 Q_{bep}$ condition, the second main frequency appeared at 8 or 12 times the rotating frequency, the

hub was affected by abundant low-frequency pulsation, and the middle point of the flow channel and the rim were affected by integer rotating frequency.

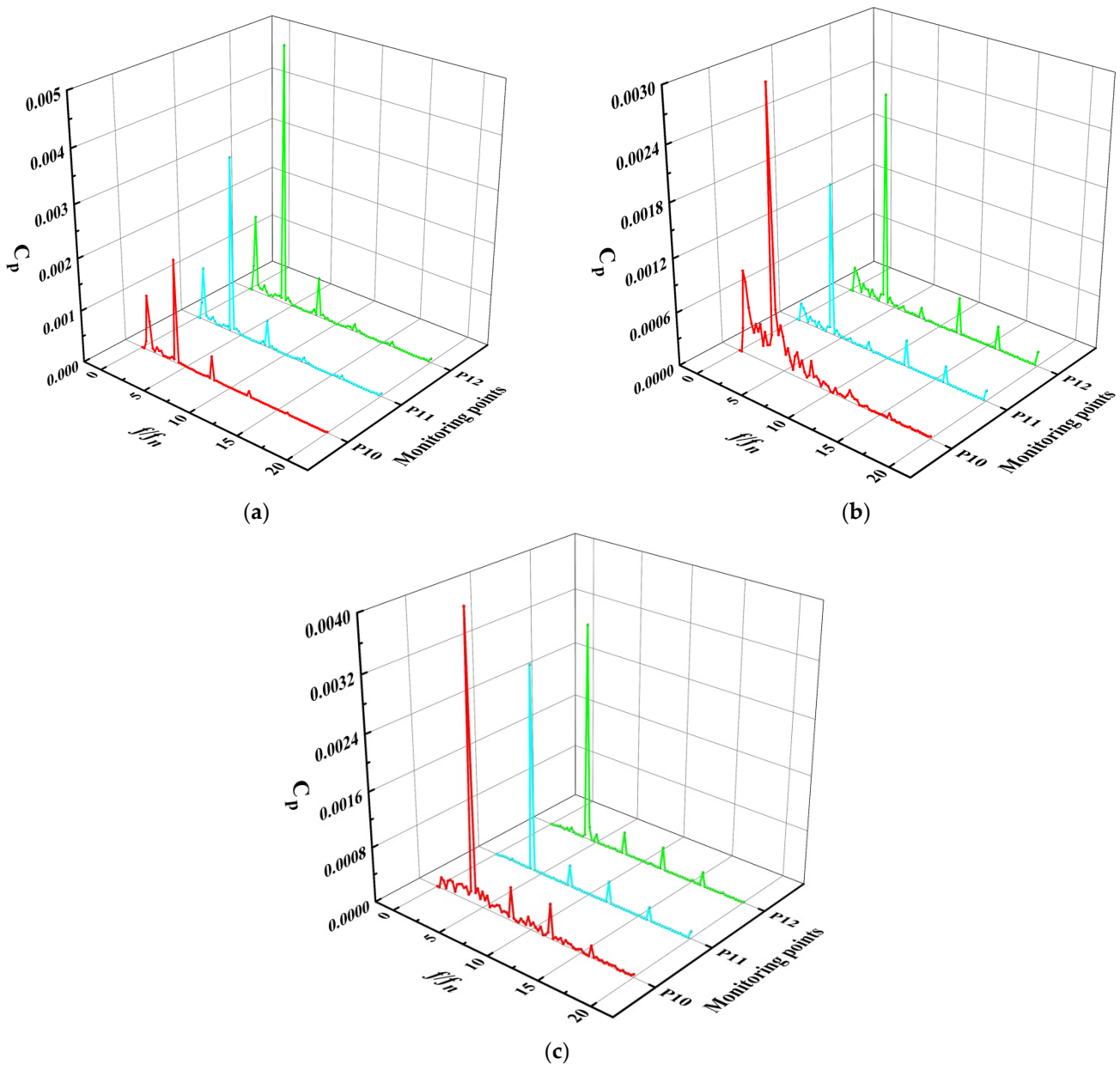


Figure 19. Spectra of pressure fluctuation at impeller outlet: (a) $0.8 Q_{bep}$, (b) $1.0 Q_{bep}$, (c) $1.2 Q_{bep}$.

Figure 20 shows the pressure fluctuation spectra of each monitoring point at the guide vane outlet under different flow conditions. Under the conditions of small flow rate and $1.0 Q_{bep}$, the main frequency of pressure pulsation at each monitoring point was not 4 times the rotating frequency, indicating that the amplitude of pressure pulsation was less affected by the number of impeller blades and the section was mainly subjected to low-frequency pulsation. After the rectification and energy recovery of the guide vane, the pressure pulsation amplitude at the outlet of the guide vane decreased. Under the condition of $0.8 Q_{bep}$, the pressure pulsation amplitude at the hub was the largest, and the main frequency was 0.75 times the rotating frequency, which was 1.88 times that at the midpoint of the flow channel. The main frequency at the rim was 1.0 times the rotating frequency. Under the condition of $1.0 Q_{bep}$, the pressure pulsation amplitude at the center of the channel was the largest, and the main frequency was 0.5 times the frequency.

Under the $1.2 Q_{bep}$ condition, the main frequency of pressure pulsation at each monitoring point was 4 times the rotating frequency, and the position of the rim was also affected by the number of impellers. The pressure pulsation at the hub was dominated by low frequencies, and the amplitude of low-frequency pulsation at the rim and the middle of the flow channel was greatly reduced. The law of pressure pulsation was similar to those of the inlet and outlet sections of the impeller, and the high-frequency pressure pulsation was at the integral frequency.

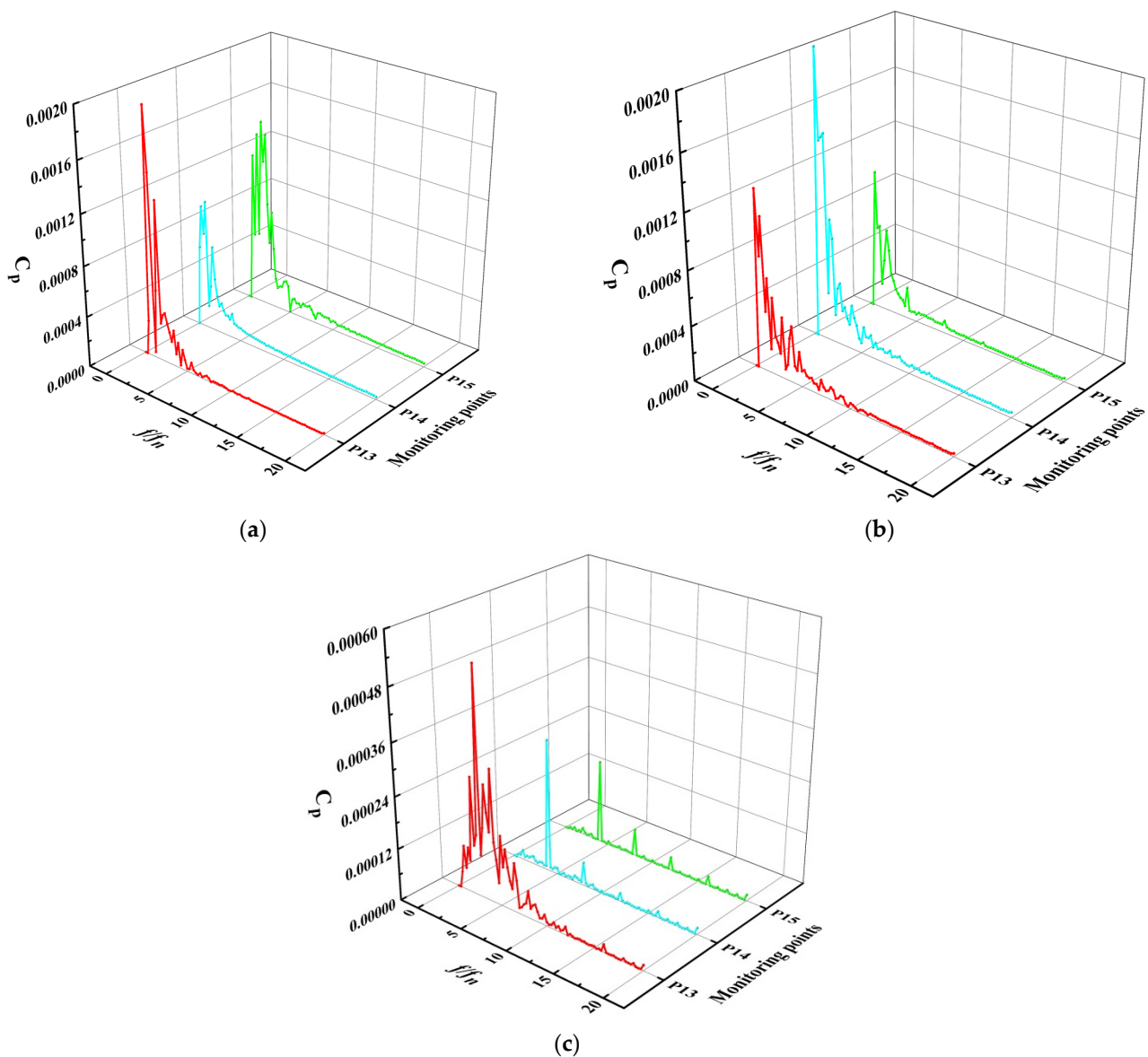


Figure 20. Spectra of pressure fluctuation at guide vane outlet: (a) $0.8 Q_{bep}$, (b) $1.0 Q_{bep}$, (c) $1.2 Q_{bep}$.

Figures 21 and 22 show the pressure fluctuation spectra of monitoring points 16–17 and 18–19, respectively. Under the $0.8 Q_{bep}$ and $1.0 Q_{bep}$ conditions, the four monitoring points were greatly affected by low-frequency pulsation, and the corresponding frequency conversion ratio of pressure pulsation coefficient in the dominant position was within 3 times that of the frequency conversion. The amplitude of pressure coefficient of each monitoring point decreased with the increase of flow rate. The distance between monitoring points 17 and 19 and the outlet section of guide vane was large, and it was less affected by velocity circulation and elbow. The pressure coefficient amplitude of monitoring point 17 was much smaller than that of monitoring point 16, and the pressure coefficient amplitude

of monitoring point 19 was much smaller than that of monitoring point 18. Under the $1.2 Q_{bep}$ condition, the spectra of monitoring point 17 and monitoring point 19 fluctuated, and there was high-frequency fluctuation. The main frequency was still within 3 times rotating frequency, and the main frequencies of monitoring point 16 and monitoring point 18 were 4 times the rotating frequency.

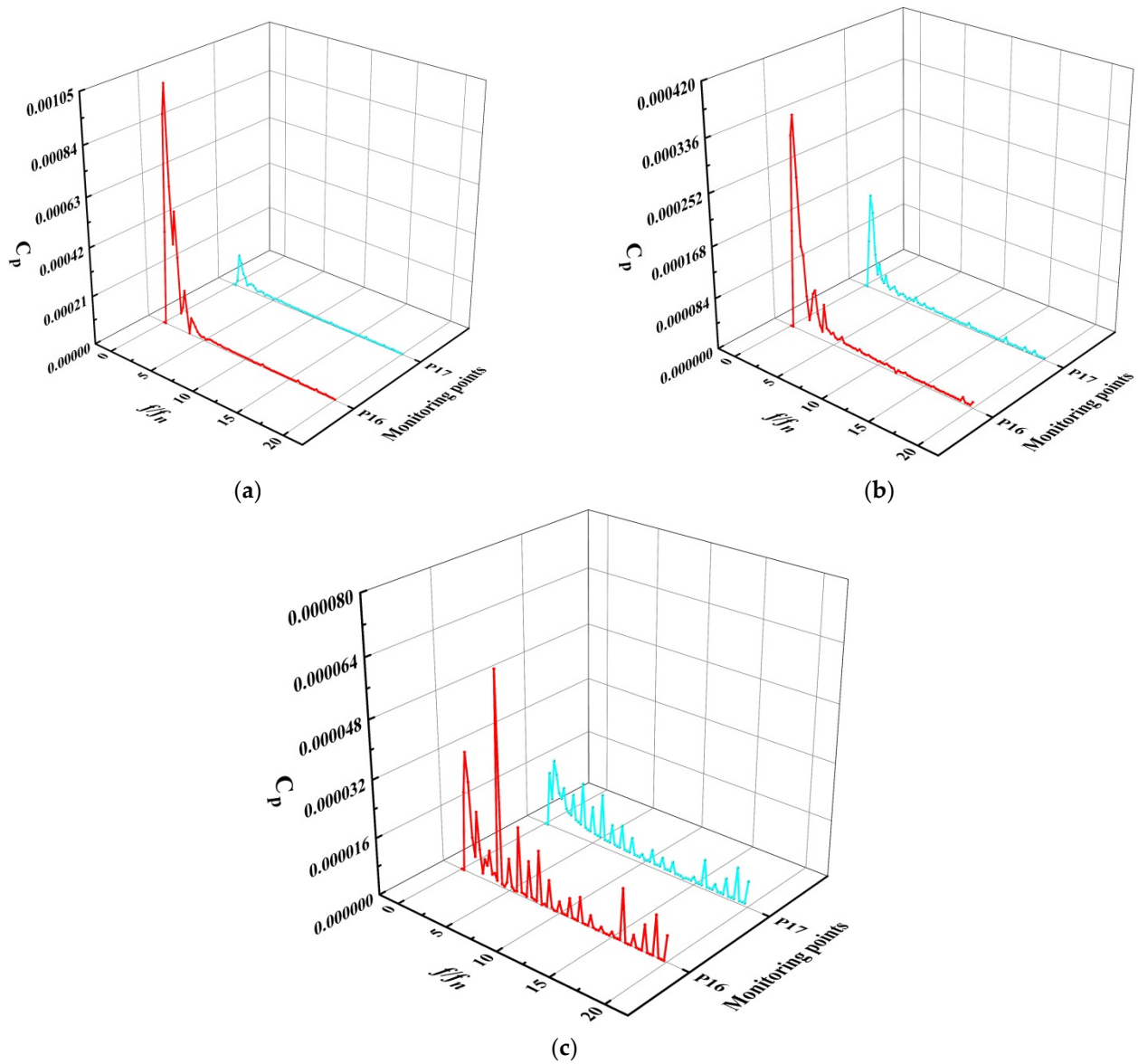


Figure 21. Spectra of pressure fluctuation at monitoring points 16–17 of straight pipe outlet flow channel: (a) $0.8 Q_{bep}$, (b) $1.0 Q_{bep}$, (c) $1.2 Q_{bep}$.

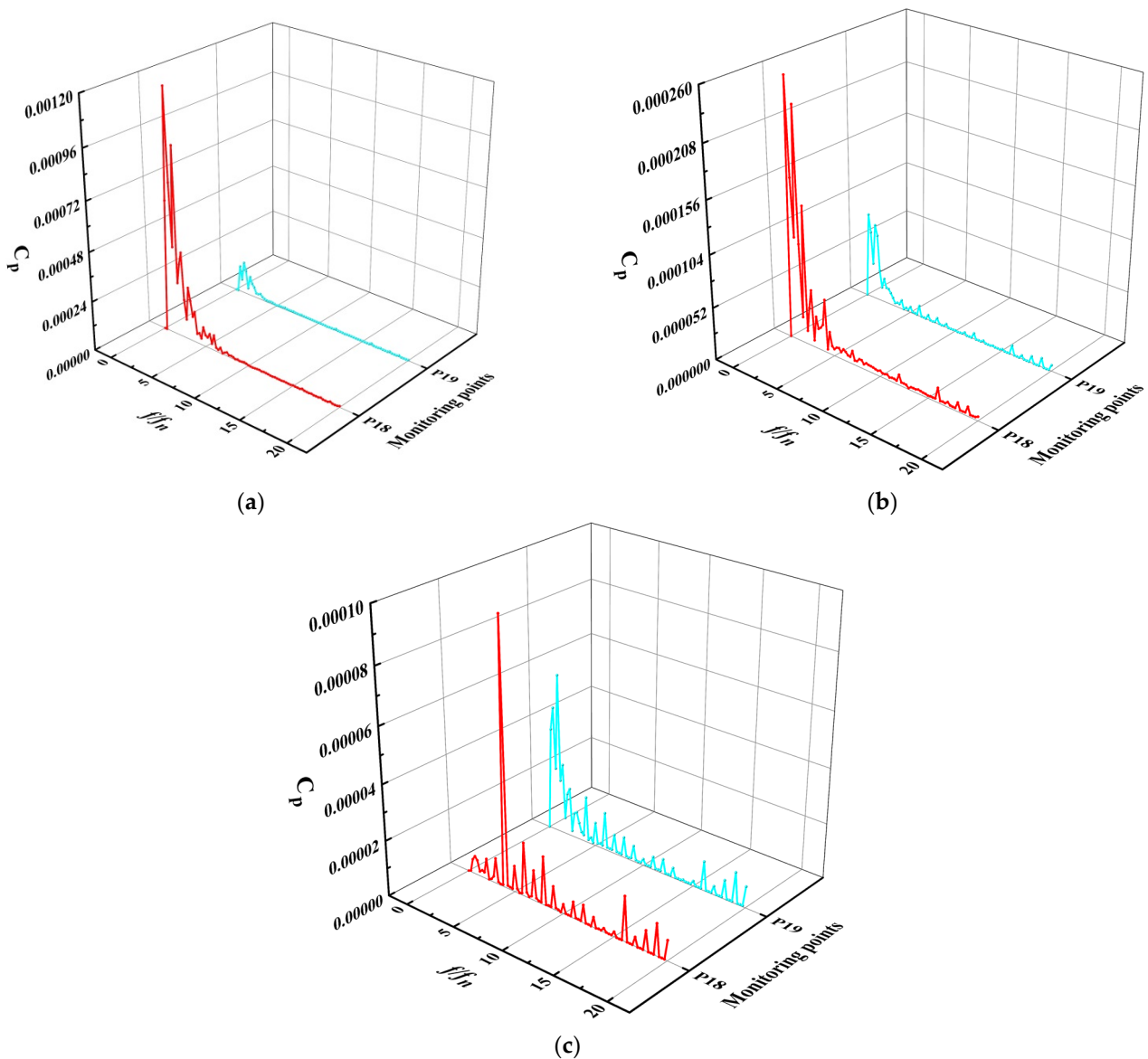


Figure 22. Spectra of pressure fluctuation at monitoring points 16–17 of straight pipe outlet flow channel: (a) $0.8 Q_{bep}$, (b) $1.0 Q_{bep}$, (c) $1.2 Q_{bep}$.

3.3. Mechanism Analysis of Pressure Pulsation

The elbow oblique inlet flow channel had a good correction of the flow pattern, and the flow pulsation was smaller than that at the impeller inlet. The main frequency distribution of the pulsation was consistent with that at the impeller inlet. The main frequency of pressure pulsation at the inlet of the impeller was 4 times the rotating frequency, because the flow pattern at the inlet of the impeller was affected by the rotation of the impeller and the flow field structure is relatively stable, so the main frequency of pressure pulsation at different measuring points changed uniformly. The pressure pulsation at the impeller outlet was due to the relative rotation between the impeller and guide vanes, and there was a large dynamic–static coupling effect, which made the pressure pulsation at the impeller outlet rich in low frequencies. The highest values of amplitudes of pressure coefficient C_p were at the relative frequency value of $f/f_n = 4.0$. This refers to the rotor blades' passing frequency. The rotor blade row had four blades. The pressure pulsation at the outlet of the guide vane originated from the velocity circulation at the outlet. Under various flow conditions, the guide vane outlet had different velocity circulations, resulting in different changes in the pressure pulsation at the outlet of the guide vane. The complexity of the outlet flow

field distribution led to low-frequency pulsation at the outlet of the guide vane, and also affected the stability of the effluent. There is a theory that the flow pulsations are caused by shedding off separated vortex structures from guide blades surfaces. A vortex street behind the guide vane trailing edge could be also considered. A detailed analysis of obtained unsteady flow results (CFD) could confirm this hypothesis. The pressure pulsation in the straight pipe outlet flow channel was small because the hydraulic pulsation induced by the flow into the guide vane after the circulation recovery and rectification was small, and the pressure pulsation at each monitoring point of the outlet was irregular due to the flow pattern distribution of the outlet.

3.4. Analysis of Peak-to-Peak Value of Pressure Pulsation

From the above analysis, it can be seen that the pressure pulsation of the pump device did not follow a pattern of simple linear growth or decrease, and there was periodic fluctuation or instability. In order to monitor the operation stability of the pump device, the concept of peak-to-peak value of pressure pulsation was introduced. The peak-to-peak value of pressure pulsation represents the variation range of pulsation signal in a period, namely the difference between the maximum value and the minimum value of the signal in a period. The confidence interval method is usually used to deal with the peak-to-peak value—that is, the interval estimation of the overall parameters is carried out and the upper and lower limits of the confidence interval are delimited, showing that the real value has a certain probability of falling around the result. The concept of confidence interval as used here is different from that in statistics. In industrial contexts, a 97% confidence interval is usually used for peak-to-peak values. The pressure fluctuation monitoring data are arranged in order of size, and the sample data of the first 1.5% and the last 1.5% are deleted. The peak-to-peak values of pressure fluctuation are obtained by subtracting the maximum and minimum values in the remaining data, rather than by determining the confidence interval according to the mean and standard deviation as in statistics.

In order to further analyze the pressure fluctuation of the impeller inlet section and the dynamic–static interference interface of the impeller guide vane and the outlet section of the guide vane of the inclined-axis extended flow pump, the peak-to-peak values of the monitoring points 7–15 were calculated. Figure 23 shows the peak-to-peak values of the pressure fluctuation for each monitoring point under different flow conditions. The peak-to-peak value of the impeller inlet section increased from the hub to the rim due to the influence of blade design. The peak-to-peak values at the middle point of the flow channel and the rim were generally higher than those at the impeller outlet section and the guide vane outlet section, indicating that the flow was affected by the impeller rotation before entering the impeller, and the flow pattern was unstable. The flow impacts the pressure surface or suction surface of the blade, resulting in a large pressure pulsation. When the flow flowed through the impeller and was affected by the guide vane rectification, the pressure gradient decreased and the pulsation pressure decreased. With the increase of flow rate, the load on the pressure surface and suction surface of the blade decreased gradually, the pressure gradient decreased, and the peak value decreased gradually. The peak value of pressure fluctuation at the hub of different sections changed little, and the peak value of pressure fluctuation at the rim of the impeller was the largest under the $1.2 Q_{\text{bep}}$ condition. The peak value at the rim of the impeller inlet reached 0.02 Pa and the peak value at the rim of the guide vane outlet was only 0.00055 Pa, which is a reduction of 97.25%. At this time, the flow pattern at the rim of the guide vane outlet was better and less affected by the impeller rotation.

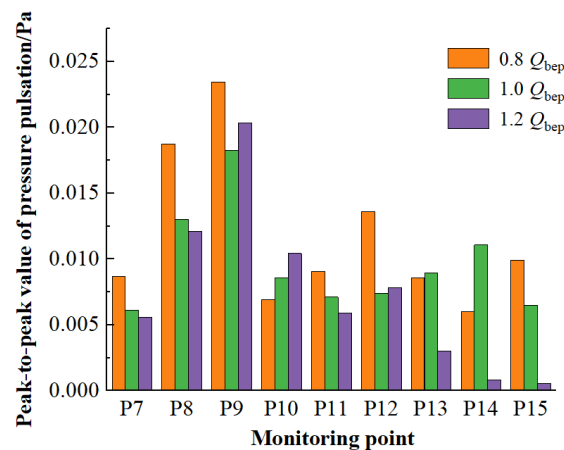


Figure 23. Peak-to-peak values of pressure fluctuation.

4. Conclusions

In this paper, a numerical simulation of a three-dimensional unsteady internal flow field and a time–frequency analysis of pressure pulsation were carried out for a 30° slanted axial-flow pump device. The main conclusions are as follows:

(1) Each monitoring point in the elbow oblique inlet flow channel had a large pressure fluctuation amplitude at 4 times the rotating frequency. The fluctuation spectra of the monitoring points inside the elbow oblique inlet flow channel were similar. Under the 1.2 Q_{bep} condition, the fluctuation of the pressure fluctuation amplitude was smaller than those under other flow conditions. The edge wall of the elbow oblique inlet flow channel was affected by the impeller rotation, and the pressure pulsation amplitude gradually increased from the inlet direction of the elbow oblique inlet flow channel to the outlet direction of the elbow oblique inlet flow channel.

(2) In a rotating cycle, there were four peaks and four troughs in the pressure pulsation on the impeller inlet section, and the amplitude of pressure pulsation increased gradually from the hub to the rim. With the increase of flow rate, the fluctuation amplitude of impeller inlet pressure fluctuation was small and tended to be stable. The main frequency of pressure pulsation at the impeller outlet was 4 times the rotating frequency, and the low frequency was rich. Under the 0.8 Q_{bep} and 1.0 Q_{bep} conditions, the pressure fluctuation of the guide vane outlet section did not show obvious regularity, and was greatly affected by low-frequency fluctuation. Under the 1.2 Q_{bep} condition, the guide vane outlet pressure fluctuation amplitude changed periodically. The peak value of the impeller inlet section increased from the hub to the rim, and the peak values at the middle point of the flow channel and the rim were higher than those of the impeller outlet section and the guide vane outlet section. With the increase of flow rate, the peak value decreased gradually.

(3) The pressure fluctuation in the elbow of the straight pipe outlet flow channel was affected by the speed loop. The main frequency of 1.2 Q_{bep} was 4 times the rotating frequency, and the amplitude of the pressure fluctuation is larger than that of the straight pipe outlet flow channel.

Author Contributions: Conceptualization, F.Y.; software and writing—original draft preparation, P.C.; writing—review and editing, F.Y. and B.M.; visualization, P.C. and Z.L.; investigation, C.L. and W.H.; supervision, C.L.; project administration, F.Y.; funding acquisition, F.Y.; All authors have read and agreed to the published version of the manuscript.

Funding: This research was funded by the National Natural Science Foundation of China (grant No. 51609210), major projects of the Natural Science Foundation of the Jiangsu Higher Education Institutions of China (grant No. 20KJA570001), the open research subject of the Key Laboratory of Fluid and Power Machinery, Ministry of Education (szjj2016-078), the Technology Project of the Water Resources Department of the Jiangsu Province (grant No. 2020029), the Scientific Research Program of Jiangsu Hydraulic Research Institute (2020z026), the Priority Academic Program Development of

the Jiangsu Higher Education Institutions (PAPD) and Postgraduate Research & Practice Innovation Program of Jiangsu Province (SJCX21_1590).

Institutional Review Board Statement: Not applicable.

Informed Consent Statement: Not applicable.

Data Availability Statement: All data necessary to carry out the work in this paper are included in the figures, tables or are available in the cited references.

Conflicts of Interest: The authors declare no conflict of interest.

References

- Rui, Z.; Chen, H. Numerical analysis of cavitation within slanted axial-flow pump. *J. Hydrodyn.* **2013**, *25*, 663–672.
- Wang, C.; Wang, F.; Tang, Y.; Zi, D.; Xie, L.; He, C.; Huang, C. Investigation Into the Phenomenon of Flow Deviation in the S-Shaped Discharge Passage of a Slanted Axial-Flow Pumping System. *J. Fluids Eng.* **2020**, *142*, 041205. [[CrossRef](#)]
- Yang, F.; Liu, C. Numerical and Experimental Investigation of Slanted Axial-flow pumping System. *J. Eng. Sci. Technol. Rev.* **2013**, *6*, 62–68. [[CrossRef](#)]
- Fu, S.; Zheng, Y.; Kan, K.; Chen, H.; Han, X.; Liang, X.; Tian, X. Numerical simulation and experimental study of transient characteristics in an axial flow pump during start-up. *Renew. Energy* **2020**, *146*, 1879–1887. [[CrossRef](#)]
- Kan, K.; Chen, H.; Zheng, Y.; Zhou, D.; Binama, M.; Dai, J. Transient characteristics during power-off process in a shaft extension tubular pump by using a suitable numerical model. *Renew. Energy* **2021**, *164*, 109–121. [[CrossRef](#)]
- Wang, Z.; Peng, G. Hydraulic performance of a large slanted axial-flow pump. *Eng. Comput.* **2010**, *27*, 243–256. [[CrossRef](#)]
- Zhang, R.; Chen, H. Influence of tip clearance on hydraulic characteristics of inclined axial flow pump. *J. Hydrodyn.* **2017**, *8*.
- Wu, C.; Tang, F.; Shi, L. Influence of guide vane position on hydraulic performance of S-type axially extended tubular pump. *J. Irrig. Drain.* **2017**, *36*, 63–69.
- Xie, R.; Tang, F.; Liu, C. Comparison of hydraulic characteristics between shaft and axially extended tubular pump. *J. Agric. Eng.* **2016**, *32*, 24–30.
- Huang, J.; Zhang, F.; Zhang, H. Orthogonal optimization design of inlet of inclined axial flow pump. *Eng. J. Drain. Irrig. Mach.* **2013**, *31*, 741–746.
- Xie, L.; Wang, F.; He, C. Experimental Study on Hydrodynamic Characteristics of 15 degree Inclined Axial Flow Pump. *J. Hydraul. Eng.* **2019**, *50*, 798–805.
- Tang, Y.; Wang, F.; Zhao, H. Study on the difference of hydraulic performance calculation of inclined axial flow pump under steady-state and transient numerical models. In Proceedings of the Mechanics and Engineering-Numerical Calculation and Data Analysis, Beijing, China, 19–21 April 2019; Volume 6.
- Wang, C.; Wang, F.; Wang, B. Research on the influence of boundary circulation distribution on numerical calculation of flow field in inclined axial flow pump outlet channel. In Proceedings of the Mechanics and Engineering-Numerical Calculation and Data Analysis, Beijing, China, 19–21 April 2019; Volume 7.
- Yang, F.; Liu, C.; Tang, F. Analysis of fluctuating characteristics of time-varying turbulent flow field in S-shaped axial extension tubular pump. *J. Hydropower* **2015**, *34*, 175–180.
- Tang, F. Design and Turbulent Numerical Analysis of Water Jet Propulsion Axial Flow Pump. Ph.D. Thesis, Shanghai Jiao Tong University, Shanghai, China, 2007.
- Yang, F.; Zhang, Y.; Yuan, Y.; Liu, C.; Li, Z.; Nasr, A. Numerical and Experimental Analysis of Flow and Pulsation in Hump Section of Siphon Outlet Conduit of Axial Flow Pump Device. *Appl. Sci.* **2021**, *11*, 4941. [[CrossRef](#)]
- Xie, C.; Tang, F.; Zhang, R.; Zhou, W.; Zhang, W.; Yang, F. Numerical calculation of axial-flow pump's pressure fluctuation and model test analysis. *Adv. Mech. Eng.* **2018**, *10*, 1687814018769775. [[CrossRef](#)]
- Shi, L.; Tang, F.; Xie, R.; Zhang, W. Numerical and experimental investigation of tank-type axial-flow pump device. *Adv. Mech. Eng.* **2017**, *9*, 1966–1970. [[CrossRef](#)]
- Izmaylov, R.A.; Lopulalan, H.D.; Norimarna, G.S. Unsteady Flow Modeling Using Transient Rotor–Stator Interface. *Turbo Expo Power Land Sea Air* **2013**, *55249*, V06CT42A039.
- Li, Y.; Zheng, Y.; Meng, F.; Osman, M.K. The Effect of Root Clearance on Mechanical Energy Dissipation for Axial Flow Pump Device Based on Entropy Production. *Processes* **2020**, *8*, 1506. [[CrossRef](#)]
- Chen, S.; Yang, F.; Huang, H. Numerical analysis of pressure pulsation in the blade area of vertical axial flow pump device. *Fluid Mach.* **2019**, *47*, 17–22.
- Jin, Y.; He, X.; Zhang, Y.; Zhou, S.; Chen, H.; Liu, C. Numerical and Experimental Investigation of External Characteristics and Pressure Fluctuation of a Submersible Tubular Pumping System. *Processes* **2019**, *7*, 949. [[CrossRef](#)]
- Roache, P.; Perspective, A. Method for Uniform Reporting of Grid Refinement Studies. *J. Fluids Eng.* **1994**, *116*, 405–413. [[CrossRef](#)]
- Zhang, H.; Sun, B.; Gao, X. Research on numerical simulation strategy of vertical inlet/outlet. *J. Hydropower* **2019**, *38*, 28–39.
- Celik, I.B.; Ghia, U.; Roache, P.J.; Freitas, C.J. Procedure for estimation and reporting of uncertainty due to discretization in CFD applications. *J. fluids Eng. Trans. ASME* **2008**, *130*, 078001.

26. Fan, Y. *Internal Flow Characteristics and Hydraulic Stability of Low-Lift Pump Device*; China Water Resources and Hydropower Press: Beijing, China, 2020.
27. Wang, F. *Flow Analysis Method of Pump and Pumping Station*; China Water Resources and Hydropower Press: Beijing, China, 2020.
28. Wu, D.; Zheng, Y.; Xue, H. Pressure pulsation characteristics of axially extended tubular pump under multiple working conditions. *J. Drain. Irrig. Mach. Eng.* **2021**, *39*, 244–250.
29. Zhang, D.; Wang, C.; Dong, Y. Experimental study on the internal pressure pulsation characteristics of a high specific speed diagonal flow pump. *J. Vib. Shock.* **2019**, *38*, 27–34.
30. Jiang, W.; Zhu, X.; Tian, H. Numerical simulation and experimental study on the influence of semi-high guide vanes on the pressure fluctuation of centrifugal pumps. *J. Cent. South Univ.* **2021**, *52*, 1276–1286.
31. Chalhoun, I.; Elaoud, S.; Kanfoudi, H.; Akrouf, M. The effects of the rotor-stator interaction on unsteady pressure pulsation and radial force in a centrifugal pump. *J. Hydrodyn. Vol.* **2018**, *30*, 672–681. [[CrossRef](#)]
32. Rydlewicz, W.; Rydlewicz, M.; Pałczyński, T. Experimental investigation of the influence of an orifice plate on the pressure pulsation amplitude in the pulsating flow in a straight pipe. *Mech. Syst. Signal Process.* **2019**, *117*, 634–652. [[CrossRef](#)]
33. He, Z. Study on Hydraulic Characteristics and Hydraulic Excitation of Large Axially Extended Tubular Pump during Transition Process. Ph.D. Thesis, Hohai University, Nanjing, China, 2018.